AIRFOIL BOUNDARY-LAYER STABILITY CALCULATIONS AND TRANSITION PREDICTION

A Thesis Submitted to
the Graduate School of Engineering and Sciences of
İzmir Institute of Technology
in Partial Fulfillment of the Requirements for the Degree of

MASTER OF SCIENCE

in Mechanical Engineering

by
Umut PEKDÜZ

July 2019
İZMİR

We approve the thesis of **Umut PEKDÜZ**

Examining Committee Members:

Assoc. Prof. Dr. Ünver ÖZKOL
Department of Mechanical Engineering, İzmir Institute of Technology

Assoc. Prof. Dr. Utku ŞENTÜRK
Department of Mechanical Engineering, Ege University
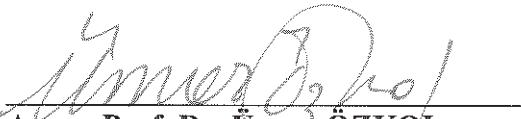
Assist. Prof. Dr. Kasım TOPRAK
Department of Mechanical Engineering, İzmir Institute of Technology

12 July 2019

Assoc. Prof. Dr. Ünver ÖZKOL
Supervisor, Department of Mechanical
Engineering, İzmir Institute of
Technology

Prof. Dr. Sedat AKKURT
Head of the Department of Mechanical
Engineering

Prof. Dr. Aysun SOFUOĞLU
Dean of the Graduate School of
Engineering and Sciences

ACKNOWLEDGMENTS

ABSTRACT

AIRFOIL BOUNDARY-LAYER STABILITY CALCULATIONS AND TRANSITION
PREDICTION

This study involves research and understanding of airfoil laminar boundary-layer transition based on three codes in written FORTRAN: panel code, boundary-layer code and stability code, namely HSPM, BLP2D and STP2D. All codes were connected to each other via inputs-outputs in the one code, called as PBS code. Firstly, the inviscid pressure distribution was obtained using Hess-Smith panel method. Secondly, differential boundary-layer equations were solved for obtained inviscid pressure distribution from panel code. Thirdly, stability calculation was performed using obtained boundary velocity profiles from boundary-layer code at each streamwise stations. Finally, the onset of transition location was predicted using e^n method based on linear small-disturbance theory. The PBS code was first validated on NACA 0012 and NACA 0015 airfoils making comparison with an experimental work in literature. After validation, three different thick airfoils designed for wind turbine applications were analyzed in terms of lift coefficient and transition location, namely NACA 64-618, DU91W250 and DU4050. The results were compared with XFoil's viscous and inviscid solutions and experimental measurements based on infrared thermography. It was seen that amplified disturbance frequency magnitude, amplification starting point and choice of threshold value are key points to correctly predict transition point for e^n method. Additionally, it was found that followings: First, as airfoil thickness increases, the need of interactive boundary-layer method increases for accurate lift coefficient; however, transition point can be still correctly predicted using inviscid pressure distribution. Second, at high angle of attacks and high Reynolds numbers, laminar boundary-layer separation point can be directly taken as transition point instead of using the e^n method.

ÖZET

KANAT KESİTİ SINIR-TABAKASININ KARARLILIK HESAPLAMALARI VE GEÇİŞ TAHMİNİ

Bu çalışma, kanat-profili laminer sınır-tabakası geçişini anlayabilmek için FOR-TRAN dilinde yazılmış üç ayrı kod üzerine kuruludur: panel kod, sınır-tabakası kodu ve kararlılık kodu, bu kodlar sırasıyla HSPM, BLP2D and STP2D'dir. Bu üç kod birbiriyle girdi-çıktı ilişkisi üzerinden PBS kod olarak adlandırılan tek bir kodda bağlanmıştır. İlk olarak, kanat-profil kesitinde Hess-Smith panel metodu kullanılarak inviskoz çözüm yapıl-mış, ikinci olarak, elde edilen basınç dağılımı ile sınır-tabakası denklemleri çözdürülerek viskoz çözüm yapılmıştır. Üçüncü olarak, akış doğrultusunda her bir istasyon için, elde edilen sınır-tabakası hız profilleri kullanılarak kararlılık denklemleri çözdürülmüş ve son olarak geçiş tahmini için doğrusal kararlılık teorisine dayanan e^n yöntemi kullanılmıştır. PBS kodu öncelikle NACA 0012 ve NACA 0015 kanat-kesitleri üzerinde sınanarak, lit-eratürdeki deneysel bir çalışma ile doğrulaması yapılmıştır. Doğrulamadan sonra, rüzgar türbini uygulamaları için özel olarak tasarlanmış kalın üç farklı kanat-profilinin, NACA 64-618, DU91W250 ve DU4050, analizleri yapılarak kaldırma katsayısı değerleri ve geçiş noktası tahminleri hücum açısına göre çizdirilmiştir. Sonuçlar XFoil'in viskoz ve inviskoz çözümleri ile kızılötesi termografiye dayanan deneysel sonuçlarla kıyaslanmıştır. Doğru bir geçiş tahmini yapabilmek için e^n geçiş tahmini yönteminde, amplifikasyon frekans büyüklüğü, amplifikasyon başlama yeri ve kritik değer seçiminin geçiş noktasını belir-lemede anahtar rol oynadığı görülmüştür. Ayrıca şu bulgular saptanmıştır: Birinci bulgu, kanat-profil kalınlığı arttıkça, gerçekçi kaldırma katsayısı değerleri için etkileşimli sınır-tabakası yönte-mine duyulan ihtiyacın arttığı, bununla birlikte, geçiş noktasının, inviskoz basınç dağılımı kullanılarak bile doğru bir şekilde tahmin edilebileceğidir. İkinci bulgu, yüksek hücum açılarında ve Reynolds sayılarında, e^n yöntemi kullanmak yerine, laminer ayrılma noktasının doğrudan geçiş noktası tahmininde kullanılabileceğidir.

TABLE OF CONTENTS

LIST OF FIGURES

LIST OF TABLES

LIST OF SYMBOLS

CHAPTER 1

PROLOGUE

1.1. Introduction

Airfoil is a cross-section of a blade and it has water drop shape. This simple geometric shape is involved in many different applications from wind turbine rotor to aircraft blade so airfoil design in terms of better aerodynamics becomes important. Many phenomena happens flow around an airfoil (See Figure 1.1). Flow stagnates at the airfoil nose, it is split to upper and lower part, it creates pressure gradients, boundary-layer develops and grows along airfoil surface, it starts as laminar regime, but it turns somehow turbulent flow, it may separate from the airfoil wall before turning the turbulent or it is reattached to the wall, and it creates wake behind the airfoil. Therefore, all phenomena must be carefully investigated and solved (if possible) for better design purposes like high lift, low drag and delayed stall performance.
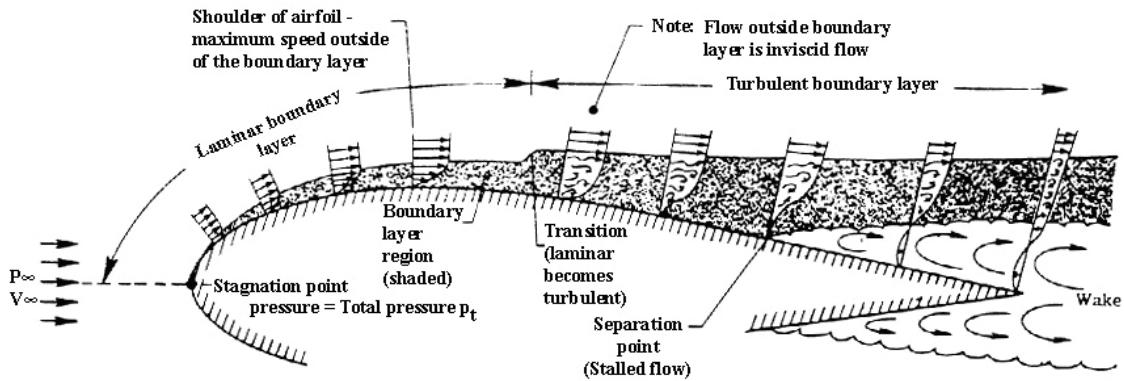
Figure 1.1. Flow around an airfoil. *Adopted fromWanthanadamkerng (2017)*

Actually, the flow over airfoil is governed by the Navier-Stokes equations, which is equation of Newtonian viscous fluid motion. The most straightforward approach is to solve directly these equations with appropriate boundary conditions. Unfortunately, there is no exist analytical solution and it requires to solve numerically with a computer but

this is very expensive, time-consuming and impracticable for 3D flow for engineering purposes. Therefore, above phenomena are separately investigated. For example, one can easily solve the equations of inviscid region to get pressure distribution, and then can obtain boundary-layer velocity profiles solving boundary-layer equations in laminar region. Using velocity profiles, stability equations can be solved and transition location can be predicted based on linear stability theory.

The knowledge of the location of transition is very important in the airfoil design. Firstly, the transition location determines the magnitude of the frictional drag because the turbulent boundary layer has higher skin-friction than its laminar boundary-layer. As clearly seen in Figure 1.2, local skin-friction coefficient values becomes lower as transition takes place further. For fully laminar case, the skin-friction has lowest magnitude but the flow is separated, which leads to very high drag. Therefore, **the aim in reducing drag is to maintain laminar flow over the large portion of airfoil avoiding separation.**
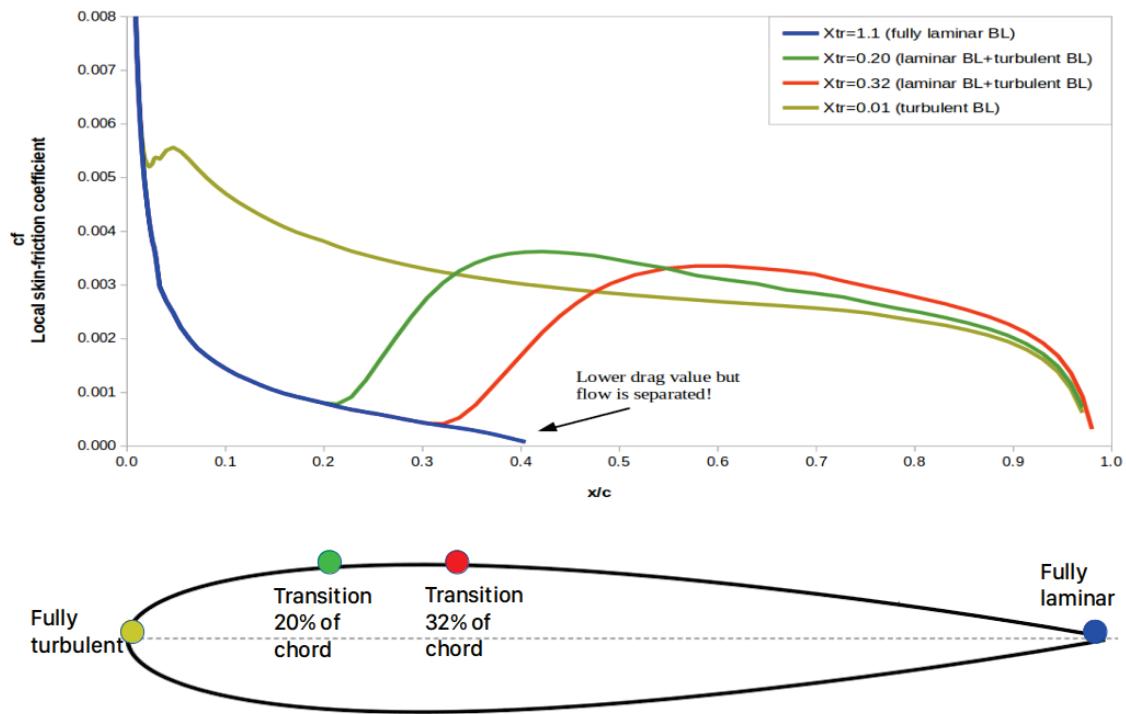
Figure 1.2. Local skin-friction distributions for various transition locations. Earlier transition means higher drag value. *Results are obtained from boundary-layer code for NACA 0012, $R = 1x10^6$, $\alpha = 2°$.*

Figure 1.3 shows total drag value as a function of transition point. As transition point moves toward the trailing edge (it means delayed transition), both total and skin-friction drag are reduced but pressure drag (or form drag) remains same. Also, as indicated the same figure, skin-friction is mainly contributing to the total drag (for small angle of attacks). Pressure drag becomes very large at stall region (at high angle of attacks). Therefore, if one wants to reduce total drag at low angle of attacks, position of the transition point must be controlled.
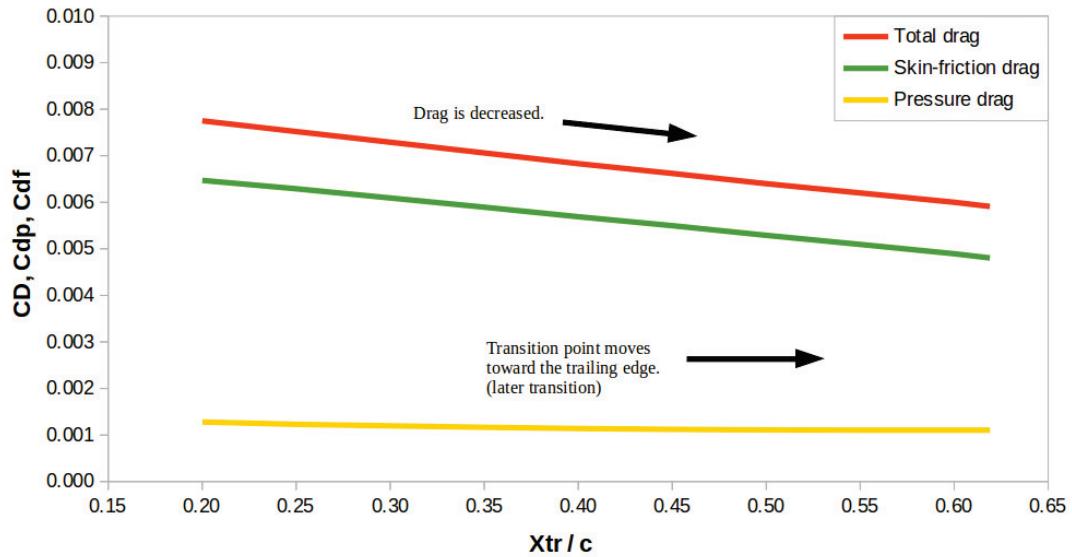
Figure 1.3. Drag coefficients as a function of transition point. *Results are obtained from XFOIL for NACA 0012, $R = 1x10^6$, $\alpha = 0°$.*

Boundary-layer profiles over an airfoil can be obtained from CFD solution for proper numerical setup. As shown in the Figure 1.4, sharp velocity changes happens inside the boundary-layer. Red color presents free-stream and above velocities (around 88 m/s), red velocity vectors are uniform but below the some point in the normal direction, velocity magnitude is decreased until the wall. It is zero at the wall (no-slip boundary condition). Blue color indicates lowest velocities at very close the wall (around 5 m/s).

In stream-wise direction, from left to right, velocity profiles change in shape. On the far left velocity profile belongs to laminar boundary-layer because of sharp parabolic shape. On the far right shape is turbulent boundary-layer since it has flat parabolic shape. (Also, see Figure 1.5). That's why, turbulent boundary-layer has higher skin-friction than laminar boundary-layer. The more results and explanation of CFD setup can be found in the Appx. B.

3
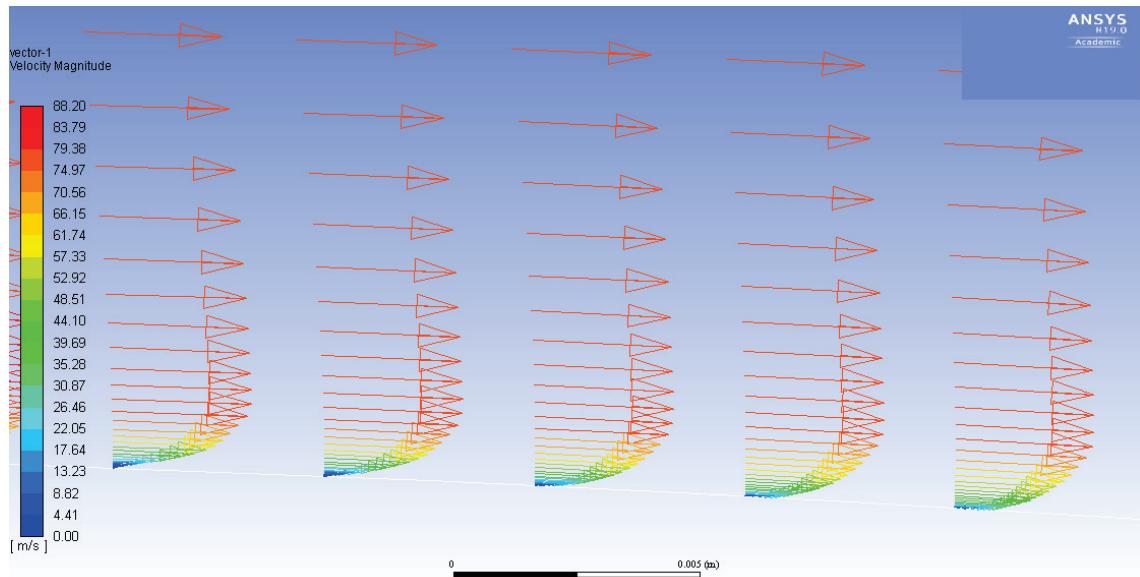
Figure 1.4. Boundary-layer velocity vectors on the airfoil. Note that there are two distinct velocity shapes. From left to right, flow is turned from laminar to turbulent. *Results from CFD simulation for DU91W250, $R = 3x10^6$, $\alpha = 8°$.*
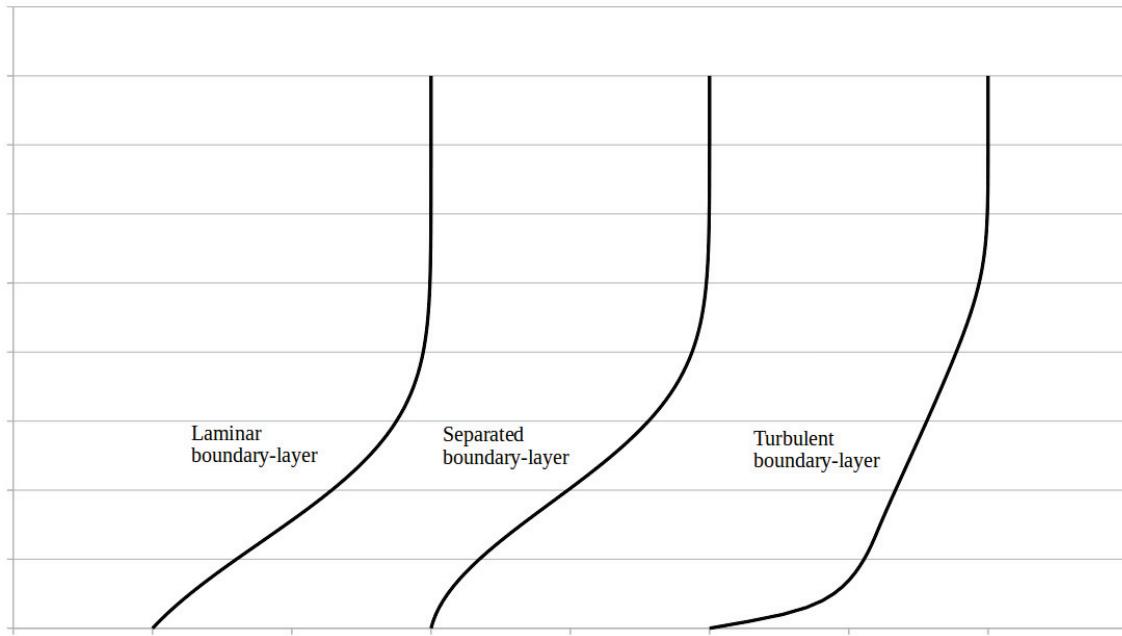
Figure 1.5. Boundary-layer velocity profiles over an airfoil. From left to right, laminar, separated and turbulent velocity profiles. *Results from boundary-layer code for DU91W250, $R = 3x10^6$, $\alpha = 0°$.*

1.2. Motivation of The Thesis

Flat plate boundary-layer solution is a well-known simple equation in fluid mechanics since the flow over flat-plate (or Blasius flow) is driven by zero pressure gradient. On the other hand, airfoil flow involves positive & negative pressure gradients. It is not possible that airfoil flow solution is given by just a simple equation. It requires numerical solution of boundary-layer equation. In addition, transition itself is complex phenomena. The physics underlying on laminar-to-turbulent transition can not be still fully understood but yet there is a very useful method to predict transition, called as e^n method. Therefore, this Master's thesis solves boundary-layer and stability equations for airfoil flow and predicts onset of transition based on e^n method. In a few words, the motivation of this Master's thesis to develop clear understanding on airfoil flow laminar boundary-layer solution and transition prediction.

1.3. Outline of The Thesis

This Master's thesis discusses mainly laminar boundary-layer transition on airfoil flow in four chapters: Chapter 1 introduces basic fluid mechanics subjects with related to airfoil flow transition. Chapter 2 provides theoretical basis of boundary-layer and stability. It involves brief derivation of laminar boundary-layer equations, detailed derivation of the Orr-Sommerfeld equation and its numerical solution, transition prediction methods and explanation and usage of e^n method. Chapter 3 presents results and discussion of five different airfoils aerodynamics characteristics in terms of lift and transition location. Chapter 4 concludes the thesis with findings and gives suggestions for further study. Appendix A provides **PBS** (**P**anel-**B**oundary layer-**S**tability) code flow diagram and explanation of the code. Appendix B gives CFD numerical setup of DU91W250 airfoil and its results. The CFD simulation was just used for illustrative purposes in introduction of Chapter 1.

CHAPTER 2

LINEAR STABILITY THEORY AND TRANSITION

This chapter starts with laminar boundary-layer equations derivation and related literature review. After an introduction to the basis of incompressible linear stability theory, the detailed study carried on *Orr-Sommerfeld equation*, which is a backbone equation for linear stability theory, presented. Derivation and some properties of the Orr-Sommerfeld equation was discussed and the numerical scheme for eigenvalue-solution was given. Finally, the chapter ends with brief explanation about transition prediction and engineering transition prediction tool: the e^n method.

2.1. Laminar Boundary-Layer Equations

Before beginning to fundamentals of stability theory, it is very convenient to derive two-dimensional laminar boundary-layer equations, explain the properties of the equations and give literature survey for numerical solutions. Since boundary-layer stability calculations require the solution of the laminar-flow boundary layer, it would be very appropriate to start derivation of the laminar boundary-layer equations.

When air flows along an airfoil surface or more generally a viscous fluid flow past a rigid surface or fixed solid wall, the essential condition is a zero relative velocity between fluid and wall (no-slip condition). If the viscosity is very small but it is not negligible, the fluid velocity changes rapidly from zero to its mainstream value at a very short distance from the wall. These narrow region adjacent to the solid surfaces, which sharp changes of velocity occur, is called *boundary layer*. As a consequence of a sharp change of the velocity, even if the viscosity itself is very small, it indicates an existence of a large gradient of shearing stress, which produces important effects on the mainstream flow.

It should be emphasized that the existence of a well-defined boundary-layer for laminar flow is a sufficiently small viscosity, and therefore sufficiently large Reynolds number but at the same time, this Reynolds number should be small enough to maintain a laminar flow.

The continuity and Navier-Stokes equations for a two-dimensional, incompressible flow can be written as (for Cartesian coordinates x,y):

$$\frac{\partial u}{\partial x} + \frac{\partial v}{\partial y} = 0 \tag{2.1a}$$

$$\frac{\partial u}{\partial t} + u\frac{\partial u}{\partial x} + v\frac{\partial u}{\partial y} = -\frac{1}{\rho}\frac{\partial p}{\partial x} + \nu\left(\frac{\partial^2 u}{\partial x^2} + \frac{\partial^2 u}{\partial y^2}\right) \tag{2.1b}$$

$$\frac{\partial v}{\partial t} + u\frac{\partial v}{\partial x} + v\frac{\partial v}{\partial y} = -\frac{1}{\rho}\frac{\partial p}{\partial y} + \nu\left(\frac{\partial^2 v}{\partial x^2} + \frac{\partial^2 v}{\partial y^2}\right) \tag{2.1c}$$

Eqs. (2.1) must be written as dimensionless form to obtain Reynolds number in the equation for employing order-of-magnitude analysis. Define the non-dimensional variables as:

$$x^* = \frac{x}{L} \qquad y^* = \frac{x}{\delta} \qquad u^* = \frac{u}{U}$$

$$v^* = \frac{v}{U}\frac{L}{\delta} \qquad p^* = \frac{p}{\rho\,U^2} \qquad t^* = t\,\frac{U}{L} \tag{2.2}$$

where L is the horizontal characteristic length, δ is the boundary layer thickness and U is the mainstream flow velocity.

Using Eqs. (2.2), the non-dimensional form of the Eqs. (2.1) can be obtained as:

$$\frac{\partial u^*}{\partial x^*} + \frac{\partial v^*}{\partial y^*} = 0 \tag{2.3a}$$

$$\frac{\partial u^*}{\partial t^*} + u^*\frac{\partial u^*}{\partial x^*} + v^*\frac{\partial u^*}{\partial y^*} = -\frac{\partial p^*}{\partial x^*} + \frac{\nu}{UL}\frac{\partial^2 u^*}{\partial(x^*)^2} + \frac{\nu}{UL}\left(\frac{L}{\delta}\right)^2\frac{\partial^2 u^*}{\partial(y^*)^2} \tag{2.3b}$$

$$\frac{\partial v^*}{\partial t^*} + u^*\frac{\partial v^*}{\partial x^*} + v^*\frac{\partial v^*}{\partial y^*} = -\left(\frac{L}{\delta}\right)^2\frac{\partial p^*}{\partial y^*} + \frac{\nu}{UL}\frac{\partial^2 v^*}{\partial(x^*)^2} + \frac{\nu}{UL}\left(\frac{L}{\delta}\right)^2\frac{\partial^2 v^*}{\partial(y^*)^2} \tag{2.3c}$$

Let define Reynolds number as:

$$R = \frac{UL}{\nu} \tag{2.4}$$

Since viscous forces balance inertia and pressure gradient inside the boundary layer, inertia and pressure terms & viscous terms should have same order in the equations.

$$\frac{\nu}{UL}\left(\frac{L}{\delta}\right)^2 = O(1) \tag{2.5}$$

For convenient, (*) sign dropped from the equation and using Eq. (2.5) and using definition of Reynolds number, Eq. (2.3) becomes:

$$\frac{\partial u}{\partial x} + \frac{\partial v}{\partial y} = 0 \tag{2.6a}$$

$$\frac{\partial u}{\partial t} + u\frac{\partial u}{\partial x} + v\frac{\partial u}{\partial y} = -\frac{\partial p}{\partial x} + \frac{1}{\mathbf{R}}\frac{\partial^2 u}{\partial x^2} + \frac{\partial^2 u}{\partial y^2} \tag{2.6b}$$

$$\frac{1}{\mathbf{R}}\left(\frac{\partial v}{\partial t} + u\frac{\partial v}{\partial x} + v\frac{\partial v}{\partial y}\right) = -\frac{\partial p}{\partial y} + \frac{1}{\mathbf{R^2}}\frac{\partial^2 v}{\partial x^2} + \frac{1}{\mathbf{R}}\frac{\partial^2 v}{\partial y^2} \tag{2.6c}$$

When Reynolds number is very large but not infinite (limit R $\rightarrow$ ∞), the Eqs. (2.6) reduce to:

$$\frac{\partial u}{\partial x} + \frac{\partial v}{\partial y} = 0 \tag{2.7a}$$

$$\frac{\partial u}{\partial t} + u\frac{\partial u}{\partial x} + v\frac{\partial u}{\partial y} = -\frac{\partial p}{\partial x} + \frac{\partial^2 u}{\partial y^2} \tag{2.7b}$$

$$-\frac{\partial p}{\partial y} = 0 \tag{2.7c}$$

In terms of the dimensional variables, the boundary-layer governing equations for two dimensional, laminar flows are:

$$\frac{\partial u}{\partial x} + \frac{\partial v}{\partial y} = 0 \tag{2.8a}$$

$$\frac{\partial u}{\partial t} + u\frac{\partial u}{\partial x} + v\frac{\partial u}{\partial y} = -\frac{1}{\rho}\frac{\partial p}{\partial x} + \nu\frac{\partial^2 u}{\partial y^2} \tag{2.8b}$$

$$-\frac{1}{\rho}\frac{\partial p}{\partial y} = 0 \tag{2.8c}$$

The required boundary conditions are:

$$y = 0, \quad u = 0 \quad v = v_w(x) \tag{2.9a}$$

$$y = \delta, \quad u = u_e(x) \tag{2.9b}$$

where u_e is edge-velocity, v_w is a transpiration velocity, which equals to zero for solid wall but non-zero for porous wall employing blowing or suction.

The important remark according to Eq. (2.8c) is that pressure is **constant** across the boundary layer. This is known as *thin-layer approximation*. Also, pressure change in x-direction, dp/dx can be written directly related to edge-velocity absorbed into boundary condition, u_e via Bernoulli's equation:

$$\frac{dp}{dx} = -\rho u_e \frac{du_e}{dx} \tag{2.10}$$

For a two-dimensional laminar flow, the momentum equation, Eq. (2.8b) and the continuity equation, Eq. (2.8a), are two equations for the two variables u, v but the Navier-Stokes equations, Eqs. (2.1), are three equations for three variables u, v and p. Because of "parabolic" nature of the boundary-layer equations, disturbances propagate only downstream and not upstream unlike "elliptical" two-dimensional Navier-Stokes equations with disturbances propagating upstream as well as downstream. The elimination of pressure as a variable and disappearing of $\partial^2 u/\partial x^2$ term allows the change in equation type from elliptical to parabolic, which greatly changes numerical computations.

The boundary layer equations as in (Eq. 2.8) are non-linear partial differential equations and it requires a numerical solution. In the pre-computer era, the integral form of boundary layer equations was given by Von Karman in his momentum integral equation. Later, Pohlhausen and Thwaites obtained an approximate solution of momentum integral equation. This gives a quick rough answer for boundary layer growth. For a special case, these partial differential equations can be reduced to a single ordinary differential equation, called Falkner-Skan Equation. The numerical solution of Falkner-Skan Equation gives similarity solution and it is usually used as initial conditions for the numerical solution of the boundary layer equation with an arbitrary pressure gradient. On the other hand, for the solution of differential form, there are two numerical methods, mostly used in literature: Crank-Nicolson Method and Keller's Box Method. A set of partial differential equations is reduced to a set of algebraic equations using both methods and it involves iterative matrix solution. Using one of these methods, one can develop a specific computer program. There are several available computer programs in the literature by Moran (1984), Panton (1996) and Cebeci and Cousteix (2005). An extensive discussion of laminar boundary layers may be found in the book of Rosenhead (1963). Schlichting and Gersten (2017)'s book (modern edition) contains detailed chapters on both laminar & turbulent boundary layers and transition.

Figure 2.1 is prepared to gain a clear overview about boundary-layer equations.

Beginning from full time-dependent Navier Stokes equations, boundary-layer equations are the reduction of Navier-Stokes equations after specific simplifications such as thin-layer approximation. For 2-D, incompressible and laminar case, Fig. 2.1 is extended with the solution of laminar boundary-layer equations. As discussed above, in the pre-computer era, Eqs. (2.8) are integrated and "momentum integral equation" is obtained by Von Karman. Momentum integral equation (single ordinary differential equation) is solved numerically by Pohlhausen and Thwaites. For the direct attempt of solving differential form, Eqs. (2.8) are firstly reduced to a single ordinary differential equation, called the Falkner-Skan equation by similarity transformation. Since the Falkner-Skan equation is homogeneous, it can be solved comparatively easily. Using a similar procedure, boundary-layer equations and their boundary conditions, respectively Eqs. (2.8) and Eqs. (2.9) can be written as a single ordinary differential equation but non-homogeneous. In computer era, different numerical methods are developed for solving the boundary-layer equations in differential form, however, the Crank-Nicolson and Keller's box methods are the most convenient ones because they allow significantly larger time steps and unconditionally stable as accuracy maintained (Cebeci and Cousteix (2005)).

Additionally, although it is out of scope of this thesis, viscid-inviscid coupling summarized as in the same Fig. 2.1. Viscid-inviscid coupling involves that flow domain is divided to two main parts: potential flow and boundary-layer flow, and it is modeled by: panel methods and solution of boundary-layer equations, respectively. Using interaction methods, it combines interactively separated flow domain and it continues to solve until a convergence is obtanied. Detailed explanation can be found in the book of Cebeci and Cousteix (2005) and in the Master thesises by Ozgen (1994), Mersinligil (2006) and Smith (2011). Also, there exists widely used a computer program by M. Drela and H. Youngren for viscous-inviscid analysis and transition prediction: XFOIL 6.99 (by year of 2013), which is interactive program for the design and analysis of subsonic isolated airfoils. Explanation on XFOIL code can be found in Drela (1989). In the fundamental paper of Drela and Giles (1987), ISES code, which is basis of XFOIL program, was explained for transonic and low Reynolds number airfoils. XFOIL uses a two-equation, integral, laminar/turbulent boundary-layer method based on dissipation closure and an Orr-Sommerfeld-based transition prediction formulation. The viscous formulation is fully coupled with the inviscid flow that is governed by a streamline-based Euler formulation. Although XFOIL is an old-school program, today, it is still widely used by researchers and designers.

Acceleration ≈ 0

Stokes Eqs.

Full time-dependent Navier-Stokes Eqs.

$\nu = 0$

Euler eqs.

Irrotational

Laplace eq.

Viscid-Inviscid Coupling

Strong Interaction (Inverse Problem)

- Quasi-simultaneous
  Veldman – Blowing velocity
- Semi-inverse
  La Balleur
- Fully simultaneous
  Drela and Giles

Weak Interaction (Standard Problem)

p(x) & ue(x) is predescribed. It allows BL separation and leads to singularity.

Average small eddies only

Large-eddy simulation eqs.

(Time) Average

Reynolds-averaged Navier-Stokes eqs. (turbulent flow)

$d\delta/dx \ll 1$

Thin-layer or parabolized turbulent Navier-Stokes eqs. (turbulent flow)

$\frac{dp}{dy}, \frac{dp}{dz} = 0$

Turbulent boundary-layer eqs.

$d\delta/dx \ll 1$

Thin-layer or parabolized laminar Navier-Stokes eqs.

$\frac{dp}{dy}, \frac{dp}{dz} = 0$

Laminar boundary-layer eqs.

2-D, incompressible

Integral Form

- Pohlausen Method
- Thwaites Method

Approximate solution of momentum integral equation

Quick rough answer for BL growth

Differential Form

- Crank-Nicolson Method
- Keller Box Method

More general and accurate but computationally more expensive

Similarity Solution

- Falkner-Skan Equation

Special flow

Figure 2.1. From Navier-Stokes equations to boundary-layer equations including viscid-inviscid coupling. *Adapted from Cebeci and Cousteix (2005)*

11

2.2. Fundamentals of Incompressible Stability Theory

In engineering fluid flows, there are two distinct flow regimes: laminar flows and turbulent flows. These two flow regimes show very different characteristics in terms of velocity profiles, momentum and heat transfer. Mostly, fluid flows are turbulent rather than laminar or it can be said that starting from laminar regime, most fluid flows somehow turn turbulence regime at certain critical Reynolds number. The most fundamental questions are: Why does turbulent flow exist? How can a laminar flow completely change to a different flow regime? Under what conditions, this change is happened? How can the location of flow regime change or namely, "*transition*" be predicted? The object of stability & transition has been studied by several researcher and it still continues as a current topic by both academic researcher and practical designers.

Let's start with the definition of "*stability*". It depends on answer of that question: Can a given physical state (e.g. laminar flow along an airfoil nose) withstand a external and internal disturbances (e.g. free-stream disturbance (external), or perturbations in boundary-layer(internal)) and the state still return to its original stand? If yes, it is stable; if not, the physical system may be unstable. That's exact job of the **small-disturbance stability analysis** to test the laminar flow against a particular disturbance (See Fig. 2.2).
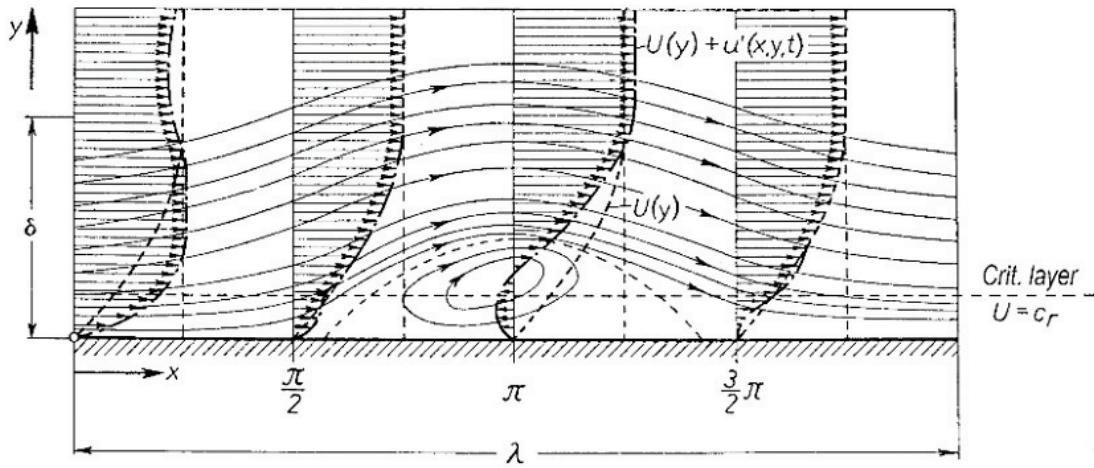
Figure 2.2. Streamline sketch of perturbation waves on a flat-plate boundary-layer at zero incidence. $U(y)$, basic flow. $U(y)+u'(y)$, perturbed velocity. *Adopted from Schlichting and Gersten (2017)*

After Prandtl's boundary-layer paper in 1904, one of the earliest investigations about viscous theory of boundary-layer instability was given by Tollmien (1929) and Schlicting (1933). However, small-disturbance linear stability theory received little acceptance until the experiment of Schubauer and Skramstad (1947). They have demonstrated appearance of instability waves in a boundary-layer, which is called Tollmien-Schlicting (TS) waves and connection with transition. After this experiment, linear theory has gained popularity. In 1956, Smith and Gamberoni, and Van Ingen was separately proposed transition prediction method based on linear stability theory as an engineering tool,which is now called as e^n method. This semi-empirical transition prediction method is still most widely used engineering approach for prediction of laminar boundary-layer transition (Mack (1984)).

As a summary, the small-disturbance theory doesn't predict any non-linear process by which triggers the flow from laminar to turbulent or nature of the turbulence. Instead, it point outs that which shapes of velocity profiles are stable or unstable, which disturbance frequencies amplify or decay in space or time, and how the parameters affect the flow to promote or delay the laminar-to-turbulence transition (Cebeci and Cousteix (2005)).

2.3. The Orr-Sommerfeld Equation

Stability analysis and transition prediction can be carried out using several approaches such as small-disturbance theory or utilizing the solutions of the unsteady Navier-Stokes equations (called direct numerical simulation, DNS) or using empirical correlations. However, most widely used one is small-disturbance theory for the stability analysis and e^n method for the transition prediction since only these are based on fast and simple engineering calculations methods. Small-disturbance stability analysis for incompressible, two-dimensional, laminar flow may be listed in following steps (White (1991)):

1) Obtain a basic solution flow, U, V and P. (in this case, the solutions of laminar boundary-layer equations)

2) Add a disturbance, û, v̂ and p̂.

3) Find the disturbance equations. (linearize if they are non-linear)

4) Select disturbance form. (in this case, a traveling wave)

5) Find the stability equation.

6) Solve the eigenvalue problem for growth or decay rates.

7) Obtain neutral stability curve and determine stability conditions.

Let's start stability analysis based on small-disturbance theory. Assume that steady solutions of Eqs. (2.8) have found: U, V and P. Define the small disturbances: $\hat{u}$, $\hat{v}$ and $\hat{p}$, superimpose on basic flow solution:

$$\bar{u} = U + \hat{u} \tag{2.11a}$$

$$\bar{v} = V + \hat{v} \tag{2.11b}$$

$$\bar{p} = P + \hat{p} \tag{2.11c}$$

Add the superimposed variables into Navier-Stokes equations. Substitute Eqs. (2.11) into Eqs. (2.1):

$$\frac{\partial(U + \hat{u})}{\partial x} + \frac{\partial(V + \hat{v})}{\partial y} = 0 \tag{2.12a}$$

$$\frac{\partial(U + \hat{u})}{\partial t} + (U + \hat{u})\frac{\partial(U + \hat{u})}{\partial x} + (V + \hat{v})\frac{\partial(U + \hat{u})}{\partial y}$$
$$= -\frac{1}{\rho}\frac{\partial(P + \hat{p})}{\partial x} + \nu\left(\frac{\partial^2(U + \hat{u})}{\partial x^2} + \frac{\partial^2(U + \hat{u})}{\partial y^2}\right) \tag{2.12b}$$

$$\frac{\partial(V + \hat{v})}{\partial t} + (U + \hat{u})\frac{\partial(V + \hat{v})}{\partial x} + (V + \hat{v})\frac{\partial(V + \hat{v})}{\partial y}$$
$$= -\frac{1}{\rho}\frac{\partial(P + \hat{p})}{\partial y} + \nu\left(\frac{\partial^2(V + \hat{v})}{\partial x^2} + \frac{\partial^2(V + \hat{v})}{\partial y^2}\right) \tag{2.12c}$$

In order to simplify Eqs. (2.12), basic flow is assumed as a **parallel-flow**, it means that $U = U(y)$ and $V = 0$. Since the steady, basic flow itself must satisfy the Navier-Stokes equations, with neglecting non-linear terms, Eqs. (2.12) can be written as:

$$\frac{\partial\hat{u}}{\partial x} + \frac{\partial\hat{v}}{\partial y} = 0 \tag{2.13a}$$

$$\frac{\partial\hat{u}}{\partial t} + U\frac{\partial\hat{u}}{\partial x} + \hat{v}\frac{dU}{dy} = -\frac{1}{\rho}\frac{\partial\hat{p}}{\partial x} + \nu\left(\frac{\partial^2\hat{u}}{\partial x^2} + \frac{\partial^2\hat{u}}{\partial y^2}\right) \tag{2.13b}$$

$$\frac{\partial\hat{v}}{\partial t} + U\frac{\partial\hat{v}}{\partial x} = -\frac{1}{\rho}\frac{\partial\hat{p}}{\partial y} + \nu\left(\frac{\partial^2\hat{v}}{\partial x^2} + \frac{\partial^2\hat{v}}{\partial y^2}\right) \tag{2.13c}$$

Eqs (2.13) are linear disturbance equations for $\hat{u}$, $\hat{v}$ and $\hat{p}$. U and dU/dy are known values and no more than variable coefficients.

The disturbances are assumed to be a single partial perturbations (or modes) and each mode is a wave propagating which has an amplitude varies in y-axis. Using complex notation, the disturbances can be written as:

$$\hat{u} = u(y)\, exp[i\,\alpha\,(x - ct)] \tag{2.14a}$$

$$\hat{v} = v(y)\, exp[i\,\alpha\,(x - ct)] \tag{2.14b}$$

$$\hat{p} = p(y)\, exp[i\,\alpha\,(x - ct)] \tag{2.14c}$$

where α is wave number, c is propagation speed, ω is wave frequency, $\omega = \alpha c$. This disturbance wave is called as *Tollmien-Schlicting wave*, which is the first sign of the laminar-flow instabilities. If Eqs. (2.14) is substituted into Eqs. (2.13) and taking derivatives, the following linear ordinary differential equations with complex coefficients are obtained:

$$i\alpha u + v' = 0 \tag{2.15a}$$

$$i\alpha u(U - c) + U'v' = -\frac{i}{\rho}\alpha p + \nu(u'' - \alpha^2 u) \tag{2.15b}$$

$$i\alpha v(U - c) = -\frac{1}{\rho}\alpha p' + \nu(v'' - \alpha^2 v) \tag{2.15c}$$

Eqs. (2.15) are two-dimensional, parallel, linear disturbances equations in terms of wave number, α and propagation speed, c. Prime denotes differentiation with respect to y. Before starting to manipulation of disturbances equations to find the Orr-Sommerfeld equation, the following question may arise: Why didn't we select disturbances as a three-dimensional wave instead of two-dimensional wave or how do we make sure that two-dimensional waves are sufficient to lead the instabilities for two-dimensional flow? Answer was given by H. Squire in 1933:

Squire's Theorem. *If a growing three-dimensional disturbance can be found at a given Reynolds number, then a growing two-dimensional disturbance exists at a lower Reynolds*

number (Fielding (2008)).

According to Squire's theorem, the two-dimensional disturbances are more unstable than three-dimensional disturbances (Cebeci and Cousteix (2005)) so two-dimensional waves are the sufficient for two-dimensional flow, even if this stability analysis were carried out for three-dimensional flow, two-dimensional disturbances would be well enough for three-dimensional flow.

Eqs. (2.15) are three linear ordinary differential equations for u, v and p. Elimination of u and v gives a simple equation for the disturbance pressure fluctuation. The followings can be obtained from Eq. (2.15a):

$$u = -\frac{v'}{i\alpha}, \quad u' = -\frac{v''}{i\alpha}, \quad u'' = -\frac{v'''}{i\alpha} \tag{2.16}$$

Insert Eq. (2.16) into Eq. (2.15b) and then multiply with $-i\alpha$:

$$-i\alpha v'(U - c) + i\alpha U'v = \frac{\alpha^2}{\rho}p - \nu(v''' - \alpha^2 v') \tag{2.17}$$

Take derivative Eq. (2.15c) with respect to y:

$$i\alpha v'(U - c) + i\alpha U'v = -\frac{1}{\rho}p'' + \nu(v''' - \alpha^2 v') \tag{2.18}$$

Sum Eq. (2.17) and Eq. (2.18) and obtain the disturbance pressure fluctuation equation:

$$p'' - \alpha^2 p = -2i\alpha\rho v U' \tag{2.19}$$

Since U' is zero outside of the boundary-layer, the solution of Eq. (2.19) must be form as:

$$p(y) = a\,e^{-\alpha y} + b\,e^{\alpha y} \tag{2.20}$$

However, the disturbance pressure should vanish at infinity, when y $\rightarrow$ ∞, $p = 0$, it follows that $b = 0$.

16

$$p(y) = a\,e^{-\alpha y} \tag{2.21}$$

According to Eq. (2.21), the pressure fluctuation decays exponentially outside of the boundary-layer, but it is proportional to dU/dy inside of the boundary-layer according to Eq. (2.19).

To obtain the Orr-Sommerfeld equation, elimination of u and p from Eqs. (2.15) requires more algebraic manipulations than obtaining disturbance pressure equation. Begin with taking the derivative of Eq. (2.15b) with respect to y:

$$i\alpha u'(U - c) + i\alpha U'u + U''v + U'v' = -\frac{i}{\rho}p' + \nu(u''' - \alpha^2 u') \tag{2.22}$$

From Eq. (2.15c), leave p' alone on the left side:

$$p' = -i\alpha v\rho(U - c) + \nu\rho(v'' - \alpha^2 v) \tag{2.23}$$

Insert Eq. (2.23) into Eq. (2.22):

$$
\begin{aligned}
i\alpha u'(U - c) &+ i\alpha u U' + U''v + U'v' \\
&= -\alpha^2 v(U - c) - i\alpha\nu v'' + i\alpha^3 v\nu + \nu(u''' - \alpha^2 u')
\end{aligned}
\tag{2.24}
$$

Using Eq. (2.16), insert the u and higher derivatives into Eq. (2.24) and then some algebraic manipulations, the result is the following fourth-order linear homogeneous equation:

$$\boxed{(U - c)(v'' - \alpha^2 v) - U''v + \frac{i\nu}{\alpha}(v'''' - 2\alpha^2 + \alpha^4 v) = 0} \tag{2.25}$$

Eq. (2.25) is the fundamental equation for linear stability theory based on small-disturbance theory, which is called **the Orr-Sommerfeld equation** derived by independently by W.M. Orr (1907) and A. Sommerfeld (1908). Eq. (2.25) is written in terms of v, eliminating u and p. One can obtain the Eq. (2.25) in terms of u at the expense of relatively difficult algebra, eliminating v and p, however, the result will be the same mathematically (White (1991)).

The boundary conditions for the Orr-Sommerfeld equation are that the disturbance velocities u and v should be zero at the wall (no-slip) and at infinity (outside of the boundary-layer). Additionally, the continuity equation, Eq. (2.15a), implies $v' = 0$ for $u = 0$. Boundary conditions for the Orr-Sommerfeld equation are given by:

$$y = 0, \quad v = 0 \quad v' = 0 \tag{2.26a}$$

$$y = \infty, \quad v = 0 \quad v' = 0 \tag{2.26b}$$

Eq. (2.25) can be written as dimensionless form. Introduce the non-dimensional variables defined by:

$$x^* = \frac{x}{\delta} \qquad y^* = \frac{x}{\delta} \qquad u^* = \frac{u}{u_e} \qquad v^* = \frac{v}{u_e} \qquad U^* = \frac{U}{u_e} \qquad p^* = \frac{p}{\rho\, u_e^2}$$

$$t^* = t\,\frac{u_e}{\delta} \qquad R = \frac{u_e \delta}{\nu} \qquad \alpha^* = \alpha\delta \qquad \omega = \frac{\omega^* \delta}{u_e} \qquad c^* = \frac{c}{u_e} \tag{2.27}$$

Using Eqs. (2.27), the non-dimensional form of the Eqs. (2.25) can be obtained as:

$$(v'''' - 2\alpha^2 + \alpha^4 v) = i\alpha R(U - c)(v'' - \alpha^2 v) - i\alpha R U'' v \tag{2.28}$$

Eq. (2.28) is the dimensionless Orr-Sommerfeld equations in terms of y-comp. of perturbation velocity, v. For convenience, $''*''$ sign dropped out. Instead of solving the Eq. (2.28) for v, more general form for u and v can be obtained for closer insight into the mechanism of disturbance by introducing perturbation stream function as:

$$\psi(x, y, t) = \phi(y)\, exp[i\,\alpha\,(x - ct)] \tag{2.29}$$

where ψ is perturbation stream function, $\phi(y)$ is an disturbance amplitude function and it only depends on y, since basic flow is only dependent on y-axis. The components of perturbation velocities can be written as:

$$u = \frac{\partial \psi}{\partial y} = \phi'(y)\, exp[i\,\alpha\,(x - ct)] \tag{2.30}$$

18

$$v = -\frac{\partial \psi}{\partial x} = -\phi(y), \exp[i\,\alpha\,(x - ct)]\,i\alpha \tag{2.31}$$

Finally, the non-dimensional Orr-Sommerfeld equation in terms of v (Eq. 2.28), can be **directly** written as dimensionless Orr-Sommerfeld equation in terms of amplitude function, $\phi(y)$:

$$\phi'''' - 2\alpha^2\phi'' + \alpha^4\phi = i\alpha R(U - c)(\phi'' - \alpha^2\phi) - i\alpha RU''\phi \tag{2.32}$$

with the boundary conditions as:

$$y = 0, \quad \phi = 0 \quad \phi' = 0 \tag{2.33a}$$

$$y = \infty, \quad \phi = 0 \quad \phi' = 0 \tag{2.33b}$$

Before any attempt to solve numerically the Eq. (2.32) with the boundary conditions (Eq. (2.33)), it may be very useful to mention about temporal and spatial amplification theories and also, to discuss on some properties of the solutions of the Orr-Sommerfeld equation. The Orr-Sommerfeld equation with its boundary conditions may be solved using *temporal* or *spatial amplifications theories*. If α is real, and ω is taken as complex, then the amplitude changes with time, it is called as temporal amplification theory, in contrast, if ω is real, and α is taken as complex, then the amplitude changes with x, it is called as spatial amplification theory. The former, Schlichting and Gersten (2017), gave solution using temporal amplification theory, however, the later, Cebeci and Cousteix (2005), employed spatial amplification theory. In addition to these amplification theories, if α and ω are taken as both real, the disturbance propagates along the mean flow with constant amplitude; if α and ω are both complex, the disturbance amplitude varies in both time and space.

Temporal amplification theory:

The wave number, α is real, and the wave frequency, ω is complex. $\omega = \omega_r + i\omega_i$
The disturbance can be written as: $\psi = \phi\,exp[i(\alpha\,x - \omega_r t)]\,exp(\omega_i t)$

Since complex function, $exp(i..)$, has always trigonometric function, there will be no constant decay for values of ω_r, therefore, the only term for decay remains $exp(\omega_i t)$. Three distinctive cases are:

$$\omega_i < 0 \qquad \text{damped wave in time} \qquad (2.34a)$$

$$\omega_i = 0 \qquad \text{neutral wave in time} \qquad (2.34b)$$

$$\omega_i > 0 \qquad \text{amplified wave in time} \qquad (2.34c)$$

Spatial amplification theory:

The wave frequency, ω is real, and the wave number, α is complex. $\alpha = \alpha_r + i\alpha_i$

The disturbance can be written as: $\psi = \phi\, exp[i(\alpha_r x - \omega t)]\, exp(-\alpha_i x)$

Similarly, since complex function, $exp(i..)$, has always trigonometric function, there will be no constant decay for values of α_r, therefore, the only term for decay remains $exp(-\alpha_i x)$. Again, three distinctive cases are defined:

$$-\alpha_i < 0 \qquad \text{damped wave in space} \qquad (2.35a)$$

$$\alpha_i = 0 \qquad \text{neutral wave in space} \qquad (2.35b)$$

$$-\alpha_i > 0 \qquad \text{amplified wave in space} \qquad (2.35c)$$

From the beginning, for many years, the temporal amplification theory was used but both theories have their own advantages. In a steady mean flow, the amplitude changes only with distance, as independent of time so this is why the spatial theory gives the amplitude change in a more direct manner than the temporal theory. The temporal amplification procedure can be found in book of Schlichting and Gersten (2017). The spatial amplification procedure was given by Cebeci and Cousteix (2005). A discussion of both procedures may be found in the extensive report of Mack (1984). This thesis will follow the solution of the Orr-Sommerfeld equation based on the spatial amplification theory, since selected basic-flow is steady mean flow.

2.3.1. The Solution Properties of the Orr-Sommerfeld Equation

The Orr-Sommerfeld equation, given by Eq. (2.32) and its boundary conditions, given by Eqs. (2.33) has a solution with the real parts of strictly positive α and ω, and then the solution exists only for a certain continuous but limited sequence of Reynolds number R and the disturbance parameters α and ω (*the eigenvalues*). The mathematical problem is *an eigenvalue problem*, and for temporal and spatial amplification theory, the combinations of the eigenvalues are given in different functional form as:

$$\text{For temporal theory:} \qquad G(\alpha, \omega_r, \omega_i, R) = 0 \qquad (2.36a)$$

$$\text{For spatial theory:} \qquad F(\omega, \alpha_r, \alpha_i, R) = 0 \qquad (2.36b)$$

The eigenvalues of the Orr-Sommerfeld equation for the spatial amplification theory are plotted in (α, R) and (ω, R) planes which describe the three cases of a disturbance (damped, neutral or amplified) for a given Reynolds number R. Figure 2.3 shows a typical viscous stability curve in (α, R) and (ω, R) planes for spatial amplification theory. In both graphics, the locus of $\alpha_i = 0$ in spatial or $\omega_i = 0$ in temporal, represents the curve of neutral stability. The neutral stability curve separates the stable region from unstable region. For spatial amplification theory, in stable region where $\alpha_i > 0$, disturbance waves are damped, but in unstable region where $\alpha_i < 0$, disturbance waves are amplified and it could indicate where the onset of laminar-to-turbulence transition starts. The point on neutral stability curve where the Reynolds number R is smallest (tangent to curve of neutral stability parallel to the α-axis or ω-axis) is very special point. Because below this point (at values of Reynolds number less than this point), it is said that that all disturbances are damped or stable and no amplification is possible. The Reynolds number, as indicated by this point, is called as the *critical Reynolds number*, R_{cr}. Although Cebeci and Cousteix (2005) named as critical Reynolds number, Schlichting and Gersten (2017) called as *indifference Reynolds number*, R_{ind}, since Schlichting defines critical Reynolds number in a different manner. According to Schlichting, all transition process is completed at R_{cr}, but R_{ind} only tells that where instability starts, and it is definitely not proper to identify R_{cr} with the transition point. Figure 2.4 clearly explains this contrast. Also, it shows all stages of laminar-turbulence transition from Tollmien-Schlichting waves (T-S

waves) given by primary stability theory to formation of turbulence spot given by secondary stability theory. The Tollmien-Schlichting waves are defined as the most unstable eigen-modes of the Orr-Sommerfeld equation.
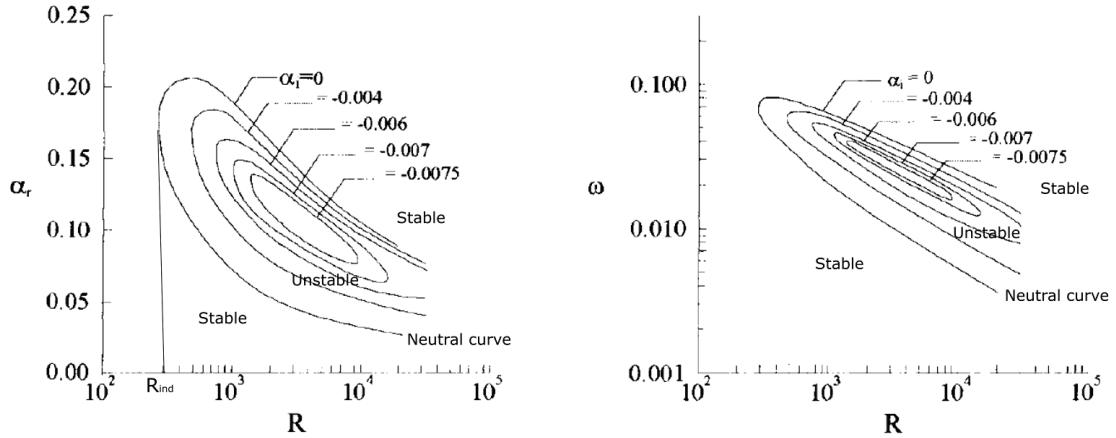
Figure 2.3. Typical stability diagrams for spatial amplification theory. *Adapted from Cebeci and Cousteix (2005)*

Sketch of laminar–to-turbulent transition in the boundary layer on a flat plate at zero incidence.

(*1*) stable laminar flow
(*2*) unstable Tollmien–Schlichting waves
(*3*) three–dimensional waves and vortex formation (Λ-structures)
(*4*) vortex decay
(*5*) formation of turbulent spots
(*6*) fully turbulent flow
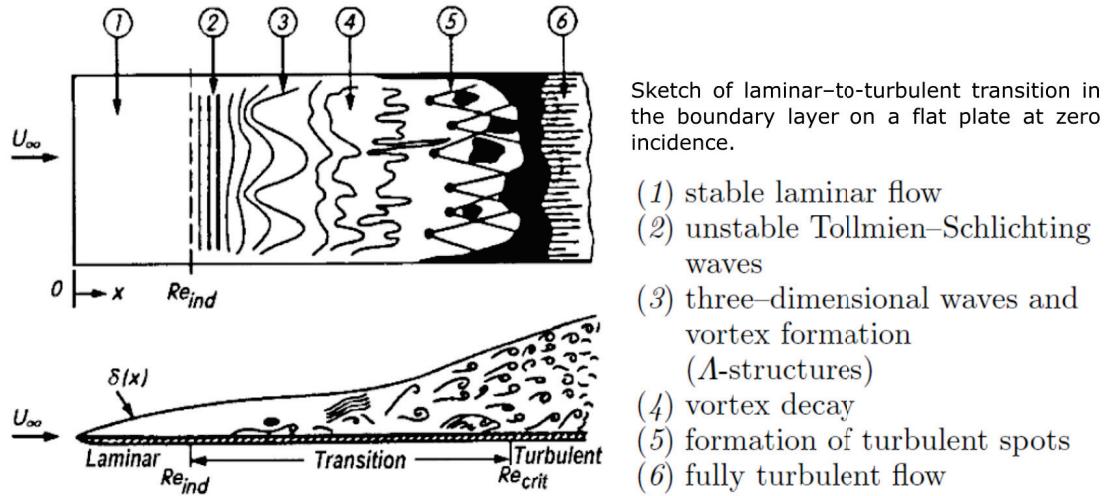
Figure 2.4. Stages of laminar-turbulent transition. Note that location of R_{ind} and R_{cr}. *Adopted from Schlichting and Gersten (2017)*

2.3.2. Inviscid Solution of the Orr-Sommerfeld Equation

Experimental results have shown that the limit of stability can be expected at high Reynolds numbers R, the Orr-Sommerfeld equation can be simplified by neglecting the friction terms on the left-hand side. Rewriting the Eq. (2.32):

$$-\frac{i}{\alpha R}(\phi'''' - 2\alpha^2\phi'' + \alpha^4\phi) = (U - c)(\phi'' - \alpha^2\phi) - U''\phi \tag{2.37}$$

when limit $R \rightarrow \infty$, left-hand side in Eq. (2.37) is zero, and then the result is inviscid perturbation equation, or also known as the Rayleigh equation:

$$(U - c)(\phi'' - \alpha^2\phi) - U''\phi = 0 \tag{2.38}$$

Since the Rayleigh equation is only of second order differential equation, only two boundary conditions are required, unlike fourth order Orr-Sommerfeld equation with four boundary conditions. The boundary-conditions for inviscid perturbation equation, Eq. (2.38), are:

$$y = 0, \quad \phi = 0 \tag{2.39a}$$

$$y = \infty, \quad \phi = 0 \tag{2.39b}$$

Earlier studies on stability theory mainly used the inviscid perturbation equation, Eq. (2.38), as a starting point in the pre-computer era rather than the more complex Orr-Sommerfeld equation. Although the important properties of the general solution of the complete perturbation equation (Eq. (2.32)) are lost in the inviscid stability theory, it leads to very important theorems given by Lord Rayleigh about the stability of laminar velocity profiles.

Theorem I. *Point of inflection criterion.* If a velocity profile has a point of inflection (see. Fig. 2.5) ($U'' = 0$), this profile is unstable. Point of inflection criterion is *a necessary and sufficient condition* for presence of unstable waves. In practice, point of inflection criterion has a great importance, because the existence of inflection point in velocity profile is directly related to the pressure gradient of the flow. Since adverse pressure gradient

where the pressure rises in the direction of mean flow ($dP/dx > 0$) has destabilize effects and favorable pressure gradient where the pressure drops in the direction of mean flow ($dP/dx < 0$) has stabilizing effects, point of inflection criterion is equivalent to the effect of the pressure gradient of the outer flow on the stability of the boundary layer. It may be said that, as a rule of thumb, the position of completed transition lies just behind the position of the pressure minimum (Schlichting and Gersten (2017)).

Theorem II. *Critical layer.* In boundary layer profiles, the velocity of propagation for neutral waves ($c_i = 0$) is smaller than the maximum velocity of the mean flow. However, if $U'' = 0$, there is at least one point, $y = y_c$, inside the boundary-layer for neutral wave where $U - c = 0$. It means that the phase velocity is equal to the mean velocity at some point inside the flow. The layer $y = y_c$ where $U = c$ is called the critical layer of the basic flow. The point, y_c is a singular point of the Rayleigh equation. The singularity indicates that the effect of viscosity in the critical layer must be considered as determining the effect of perturbation since only the effect of viscosity can handle the physically meaningless singularity of the inviscid perturbation equation, Eq. (2.38).

As a final remark to Theorem I and II, the curvature of the velocity profile is very important for the stability of laminar flow. Calculations of the laminar boundary-layer profile must be done exactly not only for $U(y)$ but also for $U''(y)$.

Figure (2.5) shows two different stability diagrams for two different velocity profiles: viscous instability and inviscid instability. Generally, type a velocity profile belongs to viscous instability diagram, type b velocity profile belongs to inviscid instability diagram. Viscous stability is the solution of the Orr-Sommerfeld equation, Eq. (2.32), however, inviscid stability is the solution of the Rayleigh equation, Eq. (2.38). From Fig. (2.5), following remarks can be made:

1. In inviscid stability diagram, unstable region is much larger than the region in viscous stability diagram. It shows that the viscosity makes contribution to stability of laminar boundary-layer.

2. At R → ∞, there still exists unstable wave-number for inviscid instability but, in viscous stability, all waves damp out at sufficient high Reynolds number R. However, it is known presence of turbulence flow in high Reynolds numbers. (See remark 5.)

3. In viscous stability, when Reynolds number is decreasing, unstable region getting larger and larger, it means that decreasing Reynolds number, or increasing viscosity can lead to instability. It appears that the viscosity does not only to damp out waves but

can actually has a destabilize effect on boundary-layer. (Compare to remark 1 and 2.)

4. For inviscid stability, velocity profile with point of inflection PI is an example of a flow of the boundary-layer in adverse pressure gradient. In inviscid stability diagram, the region, where all disturbance waves decay (below the R_{cr} or R_{ind}), is a very narrow compared to viscous stability. This is strong validation of Theorem I. (point of inflection).

5. An introduced wave into steady boundary-layer with particular frequency will continue directly as it propagates downstream and its wave-number changes. (ω = const. line in viscous stability diagram) This wave will be damped out while it passes through stable region up to R_L, the first point of neutral stability, however, it will be amplified in unstable region where between the first point of neutral stability, R_L and the second point of neutral stability, R_U. If the amplified wave is reached to the point R_U, again it will be damped out in stable region. If the amplitude of wave becomes large enough before R_U, then the nonlinear processes take place and lead to transition even though the linear theory says that it should be damped out as the wave continue to grow.
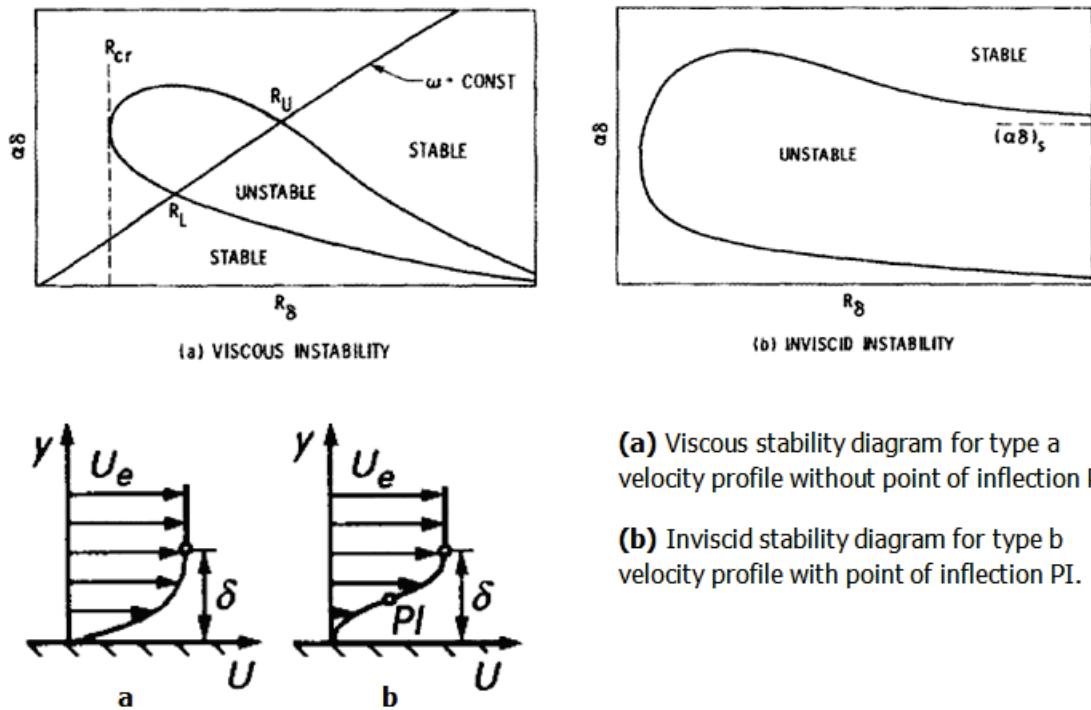
Figure 2.5. Typical neutral stability curves for viscous-inviscid stability. *Adopted from Mack (1984) and Schlichting and Gersten (2017)*

As a final step before the numerical solution of the Orr-Sommerfeld equation and its boundary conditions, the Eq. (2.32) can be written in compact form as:

$$\phi'''' - \xi_1^2 \phi'' - \xi_2^2 (\phi'' - \xi_1^2 \phi) + \xi_3 \phi = 0 \tag{2.40}$$

by defining,

$$\xi_1^2 = \alpha^2 \tag{2.41a}$$

$$\xi_2^2 = \xi_1^2 + iR(\alpha U - \omega) \tag{2.41b}$$

$$\xi_3 = iR\alpha U'' \tag{2.41c}$$

with the boundary conditions given by Eq. (2.33). On the other hand, examination of the Orr-Sommerfeld equation at the edge of the boundary-layer, in which $y = \delta$, is mathematically remarkable. Since U'' is zero, U becomes u_e and $\xi_3 = 0$ at the edge of the boundary-layer, Eq. (2.40) can be reduced to:

$$\phi'''' - \left(\xi_1^2 + \xi_2^2 \right) \phi'' + \xi_1^2 \xi_2^2 \, \phi = 0 \tag{2.42}$$

with ξ_2 evaluated at $y = \delta$. The general solution of this reduced fourth-order ordinary differential equation is given by:

$$\phi = A_1 e^{-\xi_1 y} + A_2 e^{-\xi_2 y} + A_3 e^{\xi_1 y} + A_4 e^{\xi_2 y} \tag{2.43}$$

Because the real parts of α, ξ_1 and ξ_2 require strictly positive, in order to decay boundary-layer disturbance at the edge of the boundary-layer, it is necessary that A_3 and A_4 should be zero as y $\to \delta$, $\phi \to 0$. Edge-disturbance equation is therefore reduced to:

$$\phi = A_1 e^{-\xi_1 y} + A_2 e^{-\xi_2 y} \tag{2.44}$$

Defining $D \equiv d/dy$, Eq. (2.42) can be expressed in different forms using **factorization** as:

$$\left(D^2 - \xi_1^2 \right) \left(D^2 - \xi_2^2 \right) \phi = 0 \tag{2.45a}$$

$$D^2 (D^2 - \xi_1^2) \phi - \xi_2^2 (D^2 - \xi_1^2) \phi = 0 \tag{2.45b}$$

Eqs. (2.45) implies the following boundary conditions, instead of Eqs. (2.33b):

$$(D + \xi_1) + (D + \xi_2)\phi = 0 \tag{2.46a}$$

$$(D + \xi_2) + (D^2 - \xi_1^2)\phi = 0 \tag{2.46b}$$

For clarity, note that the Orr-Sommerfeld equation, Eq. (2.32), and its boundary conditions, Eq. (2.33a) and Eq. (2.46), are given by:

$$\phi'''' - 2\alpha^2\phi'' + \alpha^4\phi = i\alpha R(U - c)(\phi'' - \alpha^2\phi) - i\alpha RU''\phi \tag{2.32}$$

with the boundary conditions as:

$$y = 0, \qquad \phi = 0 \qquad \phi' = 0 \tag{2.33a}$$

$$y = \delta, \quad (D + \xi_1) + (D + \xi_2) \ \phi = 0 \tag{2.46a}$$

$$(D + \xi_2) + (D^2 - \xi_1^2) \ \phi = 0 \tag{2.46b}$$

2.4. Numerical Solution of the Orr-Sommerfeld Equation

The first solution of the Orr-Sommerfeld equation for boundary-flow was given by Tollmien (1929) and Schlichting (1933) 20 years after the equation was derived. In pre-computer era, this was just approximate solution. In 1960s digital computer era, thanks to the direct solution of the primary differential equations, many researchers gave numerical studies on linear stability theory for different boundary-layer flows such as three-dimensional flow, compressible boundary-layers, unsteady boundary-layers and heated-wall boundary-layers. The first exact numerical solution was given by Jordinson in 1970. Detailed literature review can be found in Mack (1984).

The followed numerical solution procedure in this thesis is given by in the book of Cebeci and Cousteix (2005). The procedure of numerical solution of the Eq. (2.32) and and its boundary conditions, Eq. (2.33a) and Eq. (2.46), is based on Keller's box method, which is one of the finite-difference methods. However, there are other numerical techniques to solve the Orr-Sommerfeld equation. Mack (1984) put the available numerical methods that have been employed for the solution into three categories: finite-difference method, spectral methods and shooting methods.

Since the boundary-layer equation is parabolic type partial differential equation and the Orr-Sommerfeld equation is ordinary differential equation, usually finite-difference methods, such as Crank-Nicolson method and Keller's box method, are used for the solution. These are known as implicit method, which is the unconditionally stable and allows large time steps with high-order accuracy, unlike an explicit methods. The main advantages of the Keller's box method (also known as the box method), compare to Crank-Nicolson method, are that it has second-order accuracy for both nonuniform time and space step in expense of only slightly more arithmetic and it is capable of handling solution of large numbers of coupled equations. The numerical scheme of Keller's box method can be summarized by the following four steps:

1. Reduce the equation to a first-order system if the equation has two or higher-order.
2. Obtain difference equations using central differences. (discretization of derivatives with finite differences)
3. Linearize the resulting algebraic equations using Newton-Raphson method (or Newton method) if they are nonlinear, and write them in matrix-vector form.
4. Solve the linear system (as a matrix-vector form) by the block-tridiagonal-elimination method.

To employ the box method for formulation of numerical scheme, start with reduction of the Eq. (2.32) to a first-order system of equations. Define:

$$\phi' = f \tag{2.48a}$$

$$f' = s + \xi_1^2 \phi \tag{2.48b}$$

$$s' = g \tag{2.48c}$$

This four numerical variables, ϕ, f, s, g, are used in order to reduce a fourth-order equation to a system of equations. The compact form of the Orr-Sommerfeld equation, Eq. (2.40), can be written as:

$$g' = \xi_2^2 s - \xi_3 \phi \tag{2.49}$$

28

the boundary conditions, Eq. (2.33a), Eq. (2.46a) and Eq. (2.46b), become:

$$y = 0; \qquad \phi = 0, \qquad f = 0 \qquad\qquad (2.50a)$$

$$y = \delta; \qquad s + (\xi_1 + \xi_2)f + \xi_1(\xi_1 + \xi_2)\phi = 0 \qquad\qquad (2.50b)$$

$$g + \xi_2 s = 0 \qquad\qquad (2.50c)$$

Eqs. (2.50) are new boundary condition formulas in terms of numerical variables, ϕ, f, s, g. Box method allows nonuniform mesh as in Fig. 2.6. Between $y_0 = 0$ and $y_J = \delta$, and each grid nodes are represented by y_j, approximate finite-difference equations can be written centering around the midpoint $y_{j-1/2}$ using centered-difference derivatives for $j = 1, 2, ..., J$:
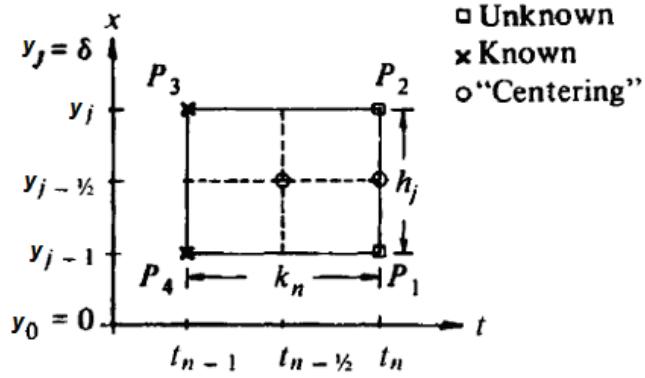
Figure 2.6. Finite-difference grid for box method. Both of h & k can be nonuniform. $y_{j-1/2} = 1/2(y_n + y_{n-1})$ *Adapted from Cebeci and Cousteix (2005)*

Eqs. (2.48) can be now written for finite-difference grid:

$$\phi_j - \phi_{j-1} - c_3(f_j + f_{j-1}) = (r_1)_j = 0 \qquad\qquad (2.51a)$$

$$f_j - f_{j-1} - c_3(s_j + s_{j-1}) - c_1(\phi_j - \phi_{j-1}) = (r_3)_{j-1} = 0 \qquad\qquad (2.51b)$$

$$s_j - s_{j-1} - c_3(g_j + g_{j-1}) = (r_2)_j = 0 \qquad\qquad (2.51c)$$

29

$$g_j - g_{j-1} - c_4(s_j + s_{j-1}) - c_2(\phi_j + \phi_{j-1}) = (r_4)_{j-1} = 0 \qquad (2.51\text{d})$$

where c_1, c_2, c_3, c_4 with $h_{j-1} = y_j - y_{j-1}$ are:

$$c_3 = \frac{h_{j-1}}{2}, \qquad c_1 = \xi_1^2 c_3, \qquad c_2 = -(\xi_3)_{j-1/2}c_3, \qquad c_4 = (\xi_2^2)_{j-1/2}c_3 \qquad (2.52)$$

the boundary conditions, Eq. (2.50)), can be written for $j = 0$ and $j = J$:

$$y = 0; \qquad \phi_0 = (r_1)_0 = 0, \qquad f_0 = (r_2)_0 = 0 \qquad (2.53\text{a})$$

$$y = \delta; \qquad f_J + \tilde{c}_3 s_J + \tilde{c}_1 \phi_J = (r_3)_J = 0, \qquad g_J + \tilde{c}_4 s_J = (r_4)_J = 0 \quad (2.53\text{b})$$

where

$$\tilde{c}_3 = \frac{1}{\xi_1 + \xi_2}, \qquad \tilde{c}_1 = \xi_1, \qquad \tilde{c}_4 = \xi_2 \qquad (2.54)$$

Since the Orr-Sommerfeld equation and the boundary conditions are homogeneous, all values of α, β, ω and R has a trivial solution $\phi(y) = 0$. To overcome this mathematically obstacle, the boundary condition, $\phi'(0) = 0$ replaced by $\phi''(0) = 1$. Now, the non-trivial solution can be obtained with adjusted boundary conditions, and then the values which satisfy original boundary condition, can be searched by Newton's method. The wall boundary conditions, Eq. (2.53a) is replaced by:

$$\phi_0 = (r_1)_0 = 0, \quad s_0 = (r_2)_0 = 1 \qquad (2.55)$$

The system of equations given by Eqs. (2.51), Eq. (2.53) and Eq. (2.55) can be written in matrix-vector form as in shown:

$$A\vec{\delta} = \vec{r} \qquad (2.56)$$

where A is a matrix, $\vec{\delta}$ and $\vec{r}$ are vector given by:

30

$$
A = \begin{bmatrix}
A_0 & C_0 & & & & & \\
B_1 & A_1 & C_1 & & & & \\
& \cdot & \cdot & \cdot & & & \\
& & B_j & A_j & C_j & & \\
& & & \cdot & \cdot & \cdot & \\
& & & & B_{J-1} & A_{J-1} & C_{J-1} \\
& & & & & B_j & A_j
\end{bmatrix}
, \quad
\vec{\delta} = \begin{bmatrix}
\delta_0 \\
\delta_1 \\
\vdots \\
\delta_j \\
\vdots \\
\delta_J
\end{bmatrix}
, \quad
\vec{r} = \begin{bmatrix}
r_0 \\
r_1 \\
\vdots \\
r_j \\
\vdots \\
r_J
\end{bmatrix}
\tag{2.57}
$$

$\vec{\delta_j}$ and $\vec{r_j}$ are defined by:

$$
\vec{\delta} = \begin{bmatrix}
\phi_j \\
s_j \\
f_j \\
g_j
\end{bmatrix}
, \quad
\vec{r_j} = \begin{bmatrix}
r_1 \\
r_2 \\
r_3 \\
r_4
\end{bmatrix}
\tag{2.58}
$$

A-matrix consists of non-scalar elements, but each element, A_j, B_j, C_j, denotes 4x4 matrices blocks (**boxes**) rather than scalars given by Eq. (2.60). That's why the method is called as Keller's box method.

In spatial-amplification theory, α is complex, ω is real and with R, the solution of the finite difference equations depends on four scalar parameters: α_r, α_i, ω and R. Eq. (2.56) can be solved for any of two scalars with remaining two scalar fixed. This dependence can be formulated as:

$$
f_0(\alpha_i, \alpha_r, \omega, R) = 0
\tag{2.59}
$$

Before the detailed eigenvalue solution procedure of Eq. (2.59) is given, this eigenvalue procedure can be summarized as:

$\alpha_i = 0$ (neutral stability), for a fixed R, calculate for α_r and ω.

$\alpha_i = 0$ (neutral stability), for a fixed α_r, calculate for R and ω.

$\alpha_i = 0$ (neutral stability), for a fixed ω, calculate for α_r and R.

for a fixed ω and for a fixed R, calculate for α_r and ω.

$$
A_0 = \begin{bmatrix} 1 & 0 & 0 & 0 \\ 0 & 1 & 0 & 0 \\ (c_1)_1 & (c_3)_1 & 0 & 0 \\ (c_2)_1 & (c_4)_1 & 0 & 0 \end{bmatrix}, \quad A_j = \begin{bmatrix} 1 & 0 & -(c_3)_j & 0 \\ 0 & 1 & 0 & -(c_3)_j \\ (c_1)_1 & (c_3)_1 & 0 & 0 \\ (c_2)_1 & (c_4)_1 & 0 & 0 \end{bmatrix}, \quad 1 \leq j \leq J-1
$$

$$
A_J = \begin{bmatrix} 1 & 0 & -(c_3)_J & 0 \\ 0 & 1 & 0 & -(c_3)_J \\ \tilde{c}_1 & \tilde{c}_3 & 1 & 0 \\ 0 & \tilde{c}_4 & 0 & 1 \end{bmatrix}, \quad j = J
$$

$$
B_j = \begin{bmatrix} -1 & 0 & -(c_3)_j & 0 \\ 0 & -1 & 0 & -(c_3)_j \\ 0 & 0 & 0 & 0 \\ 0 & 0 & 0 & 0 \end{bmatrix}, \quad 1 \leq j \leq J
$$

$$
C_j = \begin{bmatrix} 0 & 0 & 0 & 0 \\ 0 & 0 & 0 & 0 \\ (c_1)_{j+1} & (c_3)_{j+1} & -1 & 0 \\ (c_2)_{j+1} & (c_4)_{j+1} & 0 & 0 \end{bmatrix}, \quad 0 \leq j \leq J-1
$$

$$\tag{2.60}$$

Eigenvalue Procedure:

Eq. (2.59) shows two equations for a specified value of $(\alpha_i,\ R)$, with two unknowns (α_r, ω) and the equation can be solved by Newton's method. Superscript v shows known iterations, superscript $v+1$ shows next (unknown) iterations.

$$
\alpha_r^{v+1} = \alpha_r^v + \delta\alpha_r^v \tag{2.61a}
$$

$$
\omega^{v+1} = \omega^v + \delta\omega^v \tag{2.61b}
$$

For the f_r and f_i, a first-order Taylor series about α_r and ω can be written for each nonlinear equation as by taking $f_r^{v+1} = 0$ and $f_i^{v+1} = 0$. Subscripts of r and i, show real and imaginary part of f. Also, subscript of 0 dropped from f_0, for convenience.

$$f_r^v + \left(\frac{\partial f_r}{\partial \alpha_r}\right)^v \delta\alpha_r^v + \left(\frac{\partial f_r}{\partial \omega}\right)^v \delta\omega^v = 0 \tag{2.62a}$$

$$f_i^v + \left(\frac{\partial f_i}{\partial \alpha_r}\right)^v \delta\alpha_r^v + \left(\frac{\partial f_i}{\partial \omega}\right)^v \delta\omega^v = 0 \tag{2.62b}$$

The solution of a set of two linear equations with two unknowns, Eq. (2.62), is given as

$$\delta\alpha_r^v = \frac{1}{\Delta_0}\left(f_i^v \left(\frac{\partial f_r}{\partial \omega}\right)^v - f_r^v \left(\frac{\partial f_i}{\partial \omega}\right)^v\right) \tag{2.63a}$$

$$\delta\omega^v = \frac{1}{\Delta_0}\left(f_r^v \left(\frac{\partial f_i}{\partial \alpha_r}\right)^v - f_i^v \left(\frac{\partial f_r}{\partial \alpha_r}\right)^v\right) \tag{2.63b}$$

where Δ_0 is the determinant of the Jacobian of the system

$$\Delta_0 = \left(\frac{\partial f_r}{\partial \alpha_r}\right)^v \left(\frac{\partial f_i}{\partial \omega}\right)^v - \left(\frac{\partial f_i}{\partial \alpha_r}\right)^v \left(\frac{\partial f_r}{\partial \omega}\right)^v \tag{2.63c}$$

Since the vector $\vec{r}$ is independent of α_r and ω, in order to obtain the derivatives of f_r and f_i with respect to α_r and ω, differentiate Eq. (2.56):

$$A\left(\frac{\partial\vec{\delta}}{\partial\alpha_r}\right)^v = -\left(\frac{\partial A}{\partial\alpha_r}\right)^v \vec{\delta}^v = \vec{r} \tag{2.64a}$$

$$A\left(\frac{\partial\vec{\delta}}{\partial\omega}\right)^v = -\left(\frac{\partial A}{\partial\omega}\right)^v \vec{\delta}^v = \vec{r} \tag{2.64b}$$

Eqs. (2.64) is called as the variational equations of Eq. (2.56) with respect to α_r and ω. To evaluate derivatives of A with respect to α_r and ω, differentiate Eqs. (2.51).

Differentiation with respect to α_r:

$$(r_3)_{j-1} = 2\left(\frac{\partial c_1}{\alpha_r}\right)\phi_{j-1/2} \tag{2.65a}$$

$$(r_4)_{j-1} = 2\left(\frac{\partial c_4}{\alpha_r}\right)s_{j-1/2} + 2\left(\frac{\partial c_2}{\alpha_r}\right)\phi_{j-1/2} \tag{2.65b}$$

$$(r_3)_J = -\left(\frac{\partial\tilde{c}_3}{\alpha_r}\right)_J s_J - \left(\frac{\partial\tilde{c}_1}{\alpha_r}\right)_J \phi_J \tag{2.65c}$$

33

$$(r_4)_J = -\left(\frac{\partial \tilde{c}_4}{\alpha_r}\right)_J s_J \tag{2.65d}$$

Differentiation with respect to ω:

$$(r_3)_{j-1} = 0 \tag{2.66a}$$

$$(r_4)_{j-1} = 2\left(\frac{\partial c_4}{\omega}\right) s_{j-1/2} \tag{2.66b}$$

$$(r_3)_J = -\left(\frac{\partial \tilde{c}_3}{\omega}\right)_J s_J \tag{2.66c}$$

$$(r_4)_J = -\left(\frac{\partial \tilde{c}_4}{\omega}\right)_J s_J \tag{2.66d}$$

One cycle of loop iterates like this: If the initial guess values of α_r and ω don't satisfy the Eq. (2.59), the new estimate values are calculated by Newton method. From Eq. (2.64) using Eqs. (2.65) and (2.66), $\partial f/\partial \alpha_r$ and $\partial f/\partial \omega$ are obtained. Then, $\delta \alpha_r$ and $\delta \omega$ are calculated from Eqs. (2.63). The new estimate values for next iteration are calculated using Eqs. (2.61) and checked whether Eq. (2.59) is satisfied or not. The loop continues until the specified tolerance parameter is reached.

After calculation of α_r and ω for fixed R and α_i, one can formulate the numerical set up for other eigenvalue problem such as calculation of ω and R for fixed α_r. The detailed formulation can be found in Cebeci and Cousteix (2005).

The big disadvantage of the Newton method is that the method will often diverge if the initial guesses are not sufficiently close to true roots. The initial guesses are often obtained from trial and error and knowledge of the modeled physical system. For airfoil stability calculations, the initial guesses are taken from stability diagram of flat-plate solution (Blasius flow). Since Blasius flow is the solution of zero pressure gradient flow, it serves as a good starting point to estimate initial values for α and ω in the solution of pressure gradient flow.

2.5. Transition Prediction and e[n] Method

In this sub-chapter, transition phenomena is explained and transition prediction methods are reviewed. Later, e[n] method is given in detail.

2.5.1. Transition and Prediction Methods

Transition is a complicated phenomenon that involves complex physics. It includes linear & non-linear mechanism in a wide range of scales in time and length. Transition process has linear & non-linear interactions between free-stream properties (e.g., external disturbances, acoustic disturbances) and boundary-layer dynamics (e.g.,velocity profiles, instability waves).

Today, one of the most challenging engineering problem is to develop robust and reliable transition models for practical engineering flows: wind turbine blades, turbomachinery blades, aircraft, space and ground vehicles. Because of incomplete understanding of physics underlying transition process, it is impossible to include all transition mechanisms into such a simple model. In addition to this, transition modeling can not be separated from turbulence and flow separation. All phenomenons are related with each other.

The importance of transition prediction comes from practical significance in engineering designs. Transition has great influence the flow characteristic, drag losses, heat and momentum transfer. For example, in an airfoil design, it is known as a rule of thumb, the drag coefficient is decreased by 10 % when the transition point is moved 10 % of the chord toward the trailing edge (Baek and Fuglsang (2009)). Lower drag means lower fuel consumption for airplanes or more power production for wind turbine. Also, the origin of the turbulence starts with good prediction of the transition point where flow turns from laminar to turbulent.

Before giving the methods of the transition modeling, it may be useful recall and discuss the stages of a transition process:

Stage 1. Receptivity (generation of perturbations in boundary-layer)

Stage 2. Linear disturbance growth (T-S waves)

Stage 3. Non-linear interaction and secondary instabilities

Stage 4. Break-down to turbulence

This four stages describes transition phenomenon as a process. If all processes happen respectively, it is called as "*natural transition*", however, transition process has different scenarios depends on free-stream disturbances, surface roughness or boundary-layer profile. Therefore, transition can happen without taking place Stage 2. It is called

as "*bypass transition*." Bypass transition occurs at larger free-stream turbulence, usually Tu > 1%. Additionally, there is one more mode of transition called as "*separated-flow transition*". After flow is detached from the wall, it creates region where separation bubble takes place. Transition happens inside the bubble, which is known as transitional separation bubbles. After reattachment, flow totally becomes turbulent.

Although modeling of the transition process has difficulties mention above, there are available methods to predict transition point. According to Sheng (2017), this methods have been evolved into three main categories:

1. Analytical methods based on stability theory

- e^n Method

- Parabolized Stability Equations (PSE)

2. Statistical methods based on RANS equations

- Low Reynolds Number Turbulence Models

- Correlation-Based Intermittency Models

3. Transition simulation methods

- Large Eddy Simulation (LES)

- Direct Numerical Simulation (DNS)

In addition to this category, there are other prediction methods in literature: **empirical transition correlations**. The most popular one is known as Michel's criterion. This empirical criteria gives transition point as an inequality equation based on Reynolds number calculation in terms of laminar boundary-layer parameters but they are valid on only recommended Reynolds number range.

To sum up, current existing transition prediction methods vary from simple empirical correlations to expensive transition simulations. Analytical methods are based on local, linear stability equations (e^n method) or non-local, linear and non-local, non-linear stability equations (PSE). These methods don't say anything about full transition process unlike direct numerical simulation, which gives all details of transition on different modes (natural, bypass and separated) but at the same time it is very expensive tool.

Since e^n method was used in this thesis for transition prediction, more detail about this method is explained in next subchapter. For other prediction methods; more information can be found in the book of Sheng (2017). Using RANS approaches for transition prediction in a modern way can be found in the papers of Silisteanu and Botez (2010) and Russo et al. (2018).

2.5.2. e^n Method

The e^n method , which is one of the analytical methods based on stability theory, was first proposed independently by A.M.O. Smith and Van Ingen in 1956. In this method, for a given pressure distribution (from external source or using panel methods), laminar boundary-layer equations are solved and the streamwise velocity distribution u and its second derivatives u'' at each stations along the airfoil are obtained. Then, the stability properties of the velocity distributions are examined solving the Orr-Sommerfeld equation. This examination gives the total growth of boundary-layer instability modes. The basic assumption is that if the total growth exceeds some defined threshold, e^n, transition process starts. The value of n is generally taken in the range of 7 and 9. Extensive discussion about e^n method with historical review can be found in the paper of van Ingen (2008)

There are two major disadvantages related with e^n method: Firstly, the e^n methods consider only the linear growth of disturbances, namely T-S waves. Other nonlinear mechanisms are empirically included into the value of n. The method mainly predicts *onset* of natural transition. While the linear phase can extend over the long scale of the chord length, non-linear breakdown occurs very close to transition point. This can cause complete failure of the e^n method. Secondly, there is no universal constant for the value of n. It should be selected based on empirical knowledge. Specific flow conditions, disturbance environment, surface roughness or wind-tunnel turbulence intensity has large effects on value of n. For example, in the XFoil manual, it is suggested that the n-value can be taken as 10-12 for clean wind tunnel, 9 for average wind tunnel and 4-8 for dirty wind tunnel. Baek and Fuglsang (2009) suggests that n is usually set to 7 based on empirical knowledge.

To overcome one of the major shortcomings of the e^n method, Mack (1977) proposed variable n-factor methods. In this method, n-critical value is directly to the distur-

bance level and Mack suggested this formula:

$$n = -8.43 - 2.4ln(Tu) \tag{2.67}$$

In Eq. (2.67), free-stream turbulence intensity is included into the value of n. At least, one can select the true n value for wind tunnel experiment according to this formula. Also, Table 2.1 is prepared based on Mack's equation. Turbulence intensity values are taken from some wind tunnel data and papers. Table 2.1 shows that n can be taken 8 for a high quality wind tunnel where Tu is lower than 0.15%). For low quality or dirty wind tunnel (Tu>0.15%), n is suggested as 6-7. Ramanujam and Ozdemir (2017) have taken the value of 9 for their numerical works. As expected, for large turbulence intensity, n becomes smaller, it means transition occurs very soon. For the negative value of n values, they show that flow is fully turbulent from beginning for turbomachinery flow, i.e. fan, compressor, turbine blade flow), it means that there is no transition point.

Table 2.1. n-critical values for different turbulence intensity values as suggested by Mack (1977)'s equation

Tu %	N-crit Mack (1977)	Source	U (m/s)	Category	Example
0.010	14			Very low < 0.1 %	High quality wind tunnels
0.070	9	Ramanujam's paper (2017)		Very low < 0.1 %	High quality wind tunnels
0.098	8	LM Glasfiber Low Speed Wind Tunnel	50	Very low < 0.1 %	High quality wind tunnels
0.100	8	TU Delf Low Turbulence Wind Tunnel	15	Very low < 0.1 %	High quality wind tunnels
0.100	8	University of Waterloo Adaptive-Wall Wind Tunnel	2-32	Very low < 0.1 %	High quality wind tunnels
0.103	8	LM Glasfiber Low Speed Wind Tunnel	80	Very low < 0.1 %	High quality wind tunnels
0.108	8	LM Glasfiber Low Speed Wind Tunnel	100	Very low < 0.1 %	High quality wind tunnels
0.150	7	LW-2116 Wind Tunnel	0.5	Low 0.1-1 %	External flows
0.200	6	LW-2116 Wind Tunnel	1	Low 0.1-1 %	External flows
0.300	6			Low 0.1-1 %	External flows
0.400	5			Low 0.1-1 %	External flows
0.500	4			Low 0.1-1 %	External flows
1.000	3			Moderate 1-5 %	Large pipes flows
2.00	1			Moderate 1-5 %	Large pipes flows
3.00	0			Moderate 1-5 %	Large pipes flows
4.00	-1			Moderate 1-5 %	Large pipes flows
5.00	-1			High 5-20 % <	Fan, compressor, turbine flows
10	-3			High 5-20 % <	Fan, compressor, turbine flows
15	-4			High 5-20 % <	Fan, compressor, turbine flows
20	-5			High 5-20 % <	Fan, compressor, turbine flows

Fig. (2.7) explains graphically strategy of calculating the transition point with the e^n method. In α_r - R plane, the stability calculations begin at an x-location, $x = x_1$. At this point (point 1), α_r and ω are computed since u'' and R are known and the dimensional frequency ω^*, can be calculated from Eq. (2.68). This dimensional frequency is constant

along line 1. At the next location x_2 (point 2), similar to point 1 calculation, α_r and ω are computed for a new set of u'' and R and the new dimensional frequency is calculated, that is constant along line 2.

$$\omega^* = \omega \frac{u_0}{L} \qquad (2.68)$$

Before starting calculations for a new x-station, one more computation is performed. At point 1a, dimensionless frequency ω, is first calculated based on dimensional frequency on line 1 and characteristic velocity and length at point 2 from Eq. (2.69). Then with the calculated ω and specified R at point 2, α_i and α_r are computed for point 1a.

$$\omega = \omega^* \frac{L}{u_0} \qquad (2.69)$$
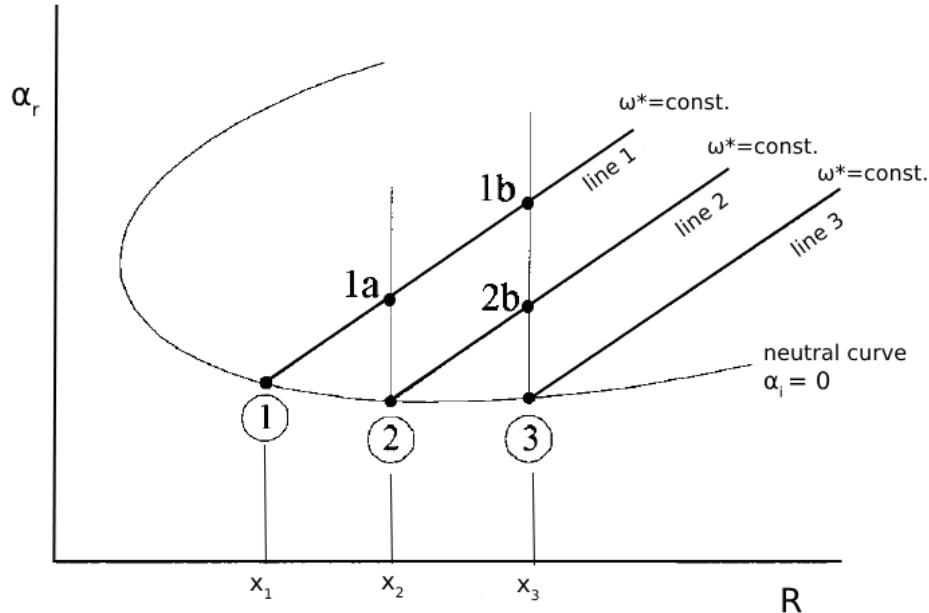
Figure 2.7. Illustration of transition point calculation for the e^n method. *Adapted from Cebeci and Cousteix (2005)*

The similar calculations are repeated at points 3, 2b and 1b. For example, at point 1b, dimensionless frequency ω, is calculated based on dimensional frequency on line 1 and characteristic velocity and length at point 3. Then with the calculated ω and specified

R at point 3, α_i and α_r are computed for point 1b. For clarity, Table 2.2 is prepared to show which variables are known or calculated at which points.

Table 2.2. Known and calculated values at different points for e^n method. *Superscript shows that which variable belongs to which point.*

	Known values	Calculated values	Calculation of ω, ω*	
Point 1	$\alpha_i=0$, R^1	α_r^1, ω^1, ω*^{1}	ω*$^1= \omega^1 (u_0^1/L^1)$	Eq. 2.68
Point 2	$\alpha_i=0$, R^2	α_r^2, ω^2, ω*^{2}	ω*$^2= \omega^2 (u_0^2/L^2)$	Eq. 2.68
Point 1a	ω^{1a}, R^2	α_i, α_r	$\omega^{1a}= \omega$*$^1 (L^2/u_0^2)$	Eq. 2.69
Point 3	$\alpha_i=0$, R^3	α_r^3, ω^3, ω*^{3}	ω*$^3= \omega^3 (u_0^3/L^3)$	Eq. 2.68
Point 2b	ω^{2b}, R^3	α_i, α_r,	$\omega^{2b}= \omega$*$^2 (L^3/u_0^3)$	Eq. 2.69
Point 1b	ω^{1b}, R^3	α_i, α_r,	$\omega^{1b}= \omega$*$^1 (L^3/u_0^3)$	Eq. 2.69

Above procedure continues for specified number of lines, typically 5 lines are enough and the variation of the integrated amplification rate n, is computed along a constant frequency line for specified number of lines. x_0 corresponds to each value of x on the neutral stability curve.

$$n = - \int_{x_0}^{x} \alpha_i dx \tag{2.70}$$

The computation of integrated amplification rate is the most crucial part of the e^n method. This leads to detection of the transition point. Depending on the selection of threshold n-value, namely n_{crit}, transition point is predicted as shown in Fig. 2.8. According to this figure, for the different values of $n = 7$, 8 and 9, transition points x_{tr} can be predicted as 0.46, 0.49 and 0.52, respectively. Note that selection of n_{crit} is arbitrary and lower n values mean earlier starting point of the transition. Fig. 2.9 shows that transition point variation with respect to different n_{crit} values and its physical frequency. Note that higher frequency values mean earlier transition beginning.
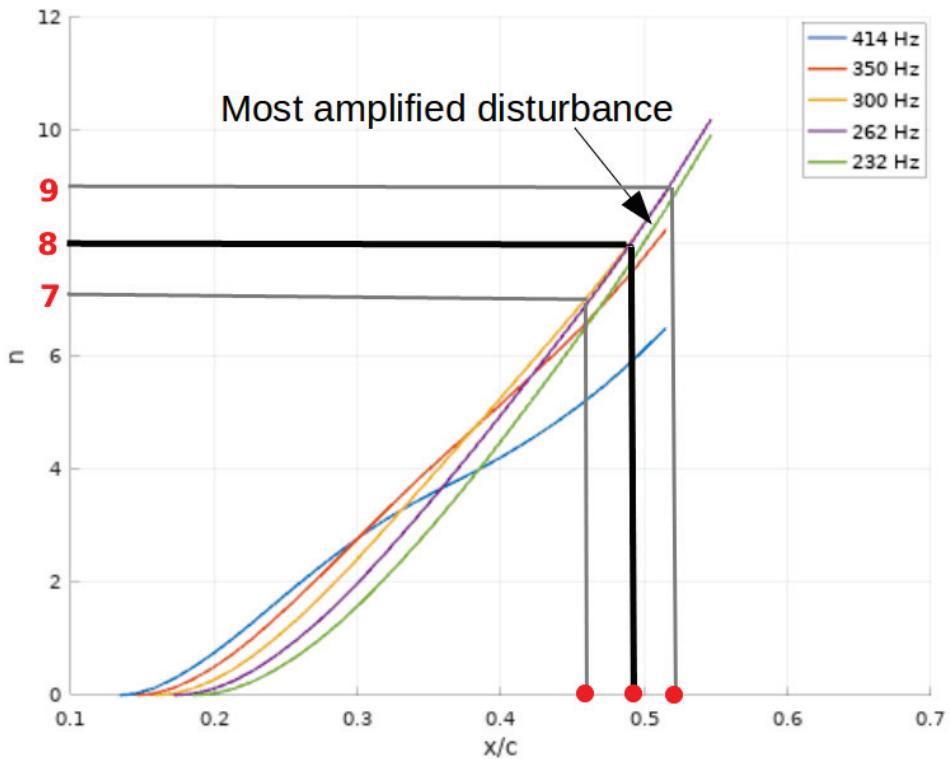
Figure 2.8. Variation of the integrated amplification rates for NACA 0012, at zero angle of attack, $R = 3x10^6$.
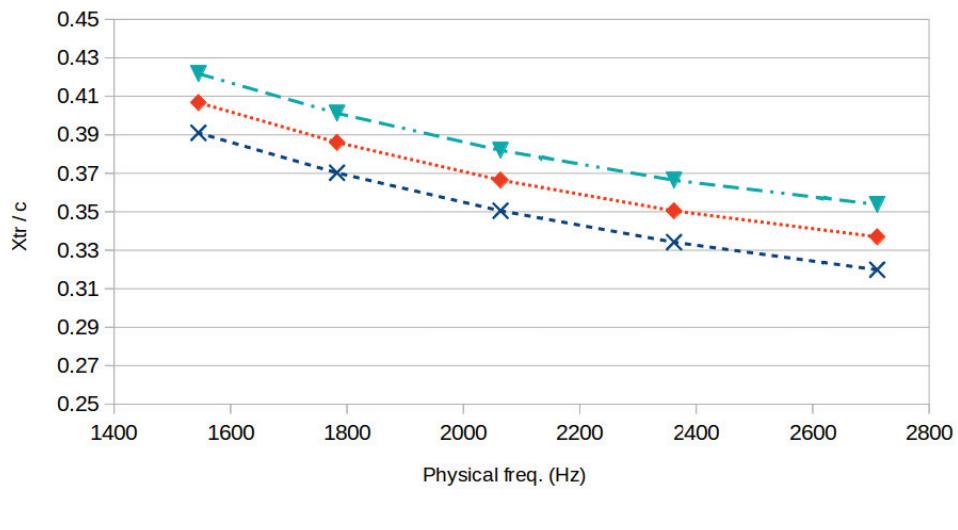

Figure 2.9. Transition point location variation with respect to its physical frequency for different n_{crit} values. NACA 0015, $\alpha = 0$, $R = 3x10^6$.

CHAPTER 3

APPLICATIONS OF PANEL-BL-STABILITY (PBS) CODE

In this chapter, the PBS code is applied on five different airfoils. For each airfoils, firstly the inviscid solution is obtained by panel code, secondly boundary-layer equation is solved for the given inviscid pressure distribution from panel code and thirdly, the stability equation is solved for obtained boundary-layer velocity profiles and transition point is predicted using e^n method. Short flow diagram of the PBS code is given Fig. 3.1. The detailed flow diagram with all inputs-outputs can be found in the Appx A.
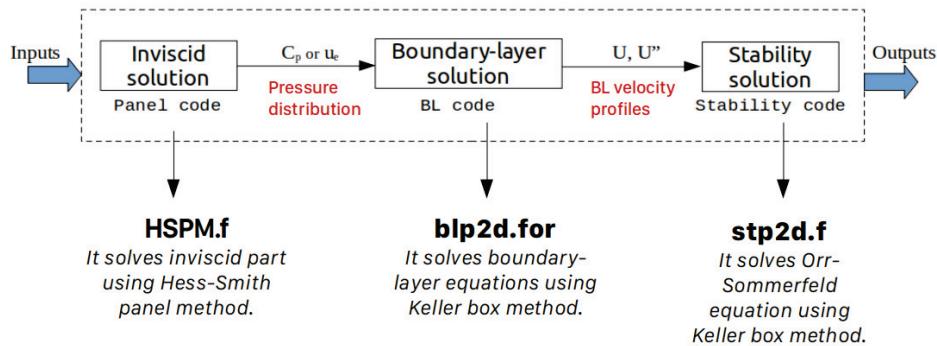
Figure 3.1. PBS code short flow diagram

To validate of the PBS code, two symmetrical NACA 4-digits airfoils (0012 and 0015) was used. The results are compared with Gregory and O'Reilly (1973)'s wind tunnel measurements. After verification, the PBS code is applied on three wind turbine airfoils. Experimental results from Baek and Fuglsang (2009)'s paper and XFoil's results are compared to the PBS code results.

3.1. NACA 4-digit Airfoils

NACA 4-digits airfoils are one of the most classical family of the NACA airfoils series, designed for general aviation applications. Although 4-digit series were used or adopted in the earlier wind turbines, today, these series are not used in modern wind tur-

bines because of their sensitivity to surface roughness (Timmer (2009)). However, NACA airfoils have very well documented aerodynamics data, so this makes them as a good reference airfoils to validate any numerical or experimental study. In this study, NACA 0012 and NACA 0015 airfoils were selected for verification of the PBS code. These two relatively thin airfoils show good behavior in terms of transition and separation characteristics since for these airfoils, transition takes place before further laminar boundary-layer separation at low-to-moderate angle of attacks.

3.1.1. NACA 0012

NACA 0012 is a symmetrical airfoil and it has 12% maximum thickness to chord ratio and no chamber (Fig. 3.2). The PBS code results are compared with experimental work of Gregory and O'Reilly (1973) and XFoil at $1.44x10^6$ and $2.88x10^6$ Reynolds numbers (Fig. 3.3 and 3.4). Both figures give similar transition points and lift coefficients despite the results are relying on different numerical methods and experimental data. Also, in Figure 3.4, it is clearly seen that both lift coefficient values are very close although PBS gives lift coefficients based on only inviscid panel method, however, XFoil's results are based on viscous-inviscid interactive method. Therefore, for thin airfoils, the inviscid methods are sufficient to give accurate lift coefficients at low-to-moderate angle of attacks (Compare with Fig. 3.13a).
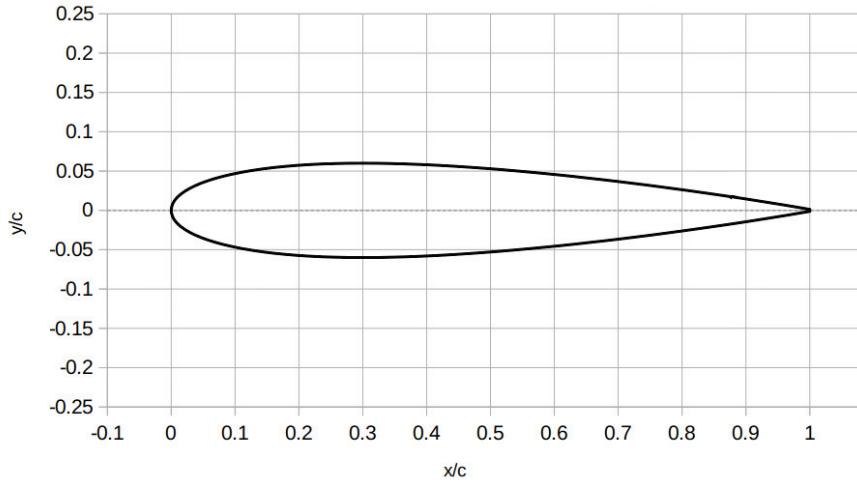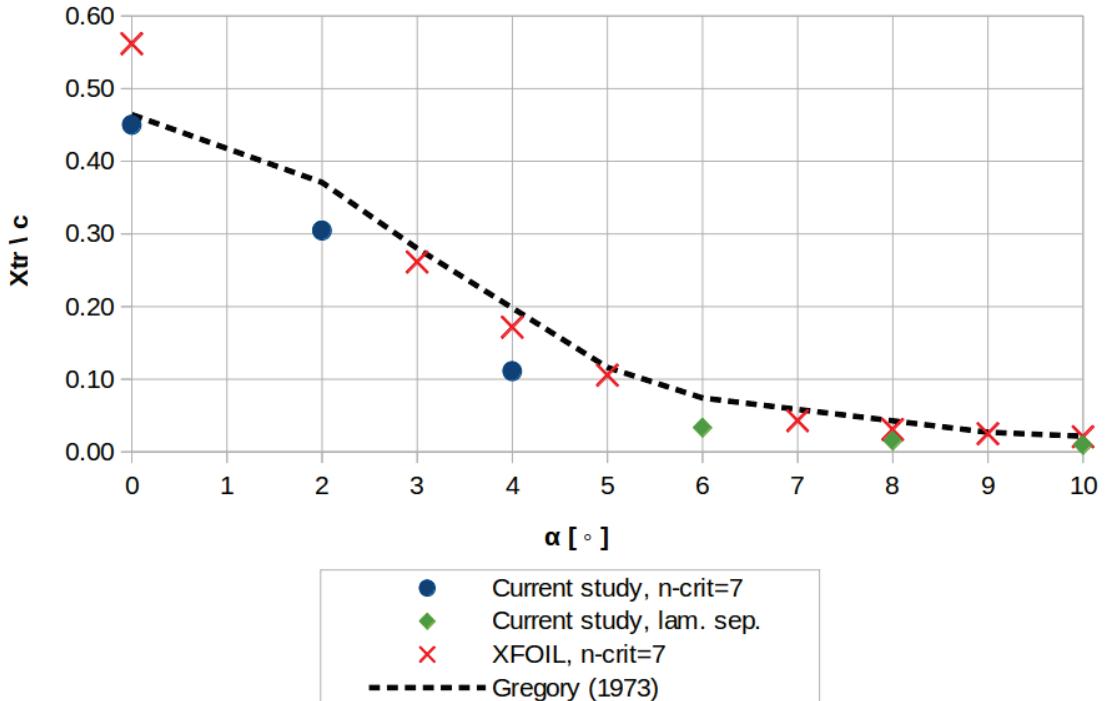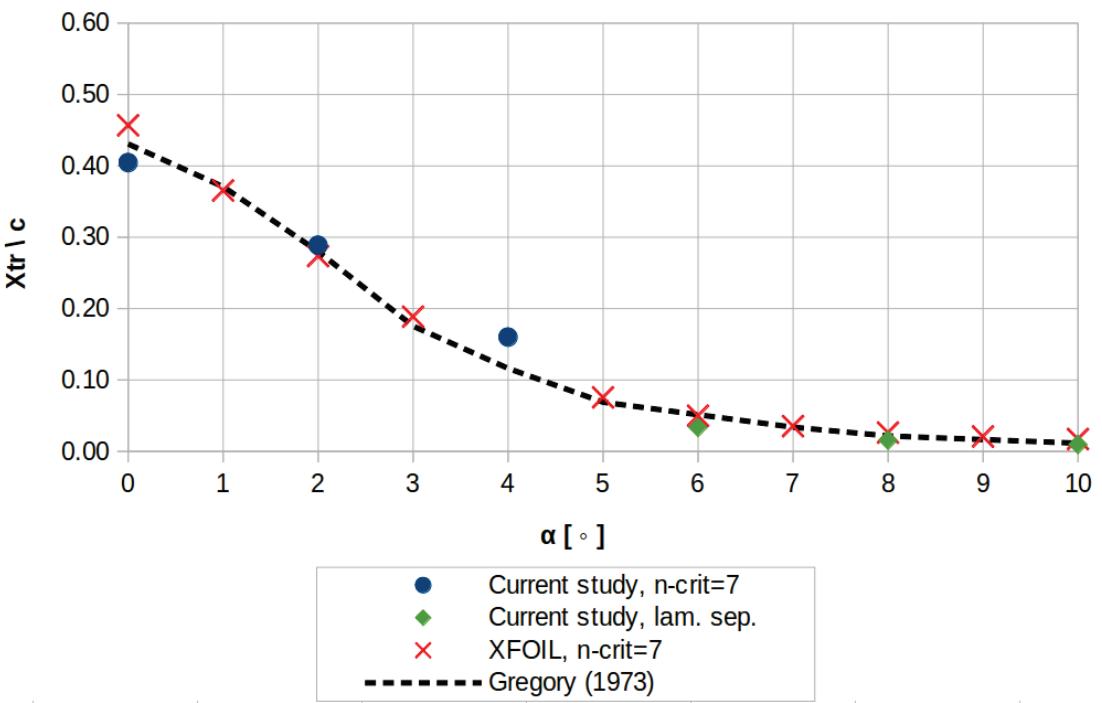


Figure 3.2. NACA 0012 Airfoil
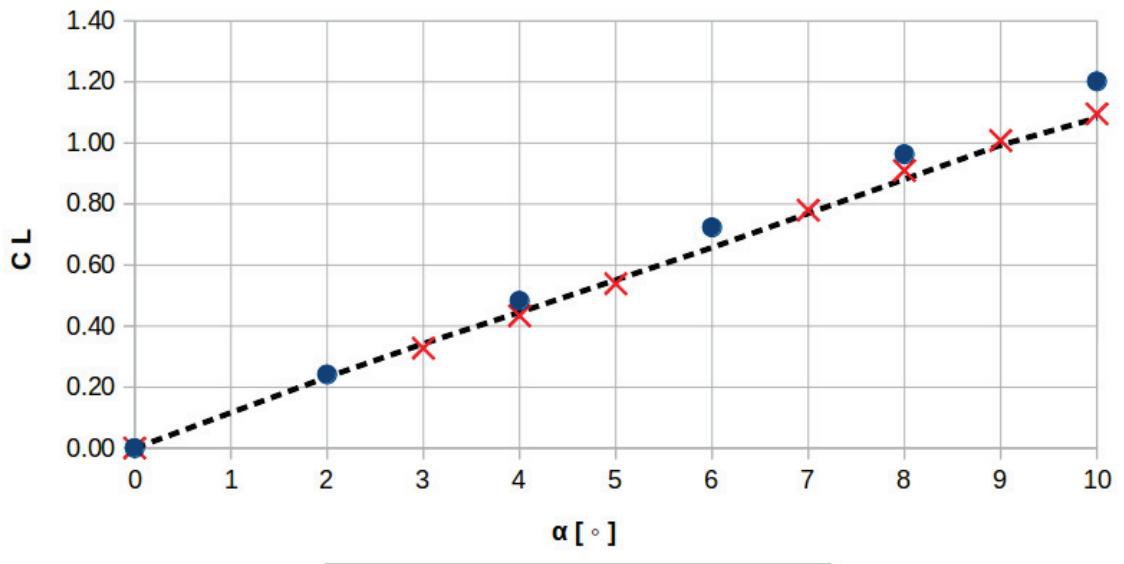
(a) NACA 0012, R=$1.44x10^6$
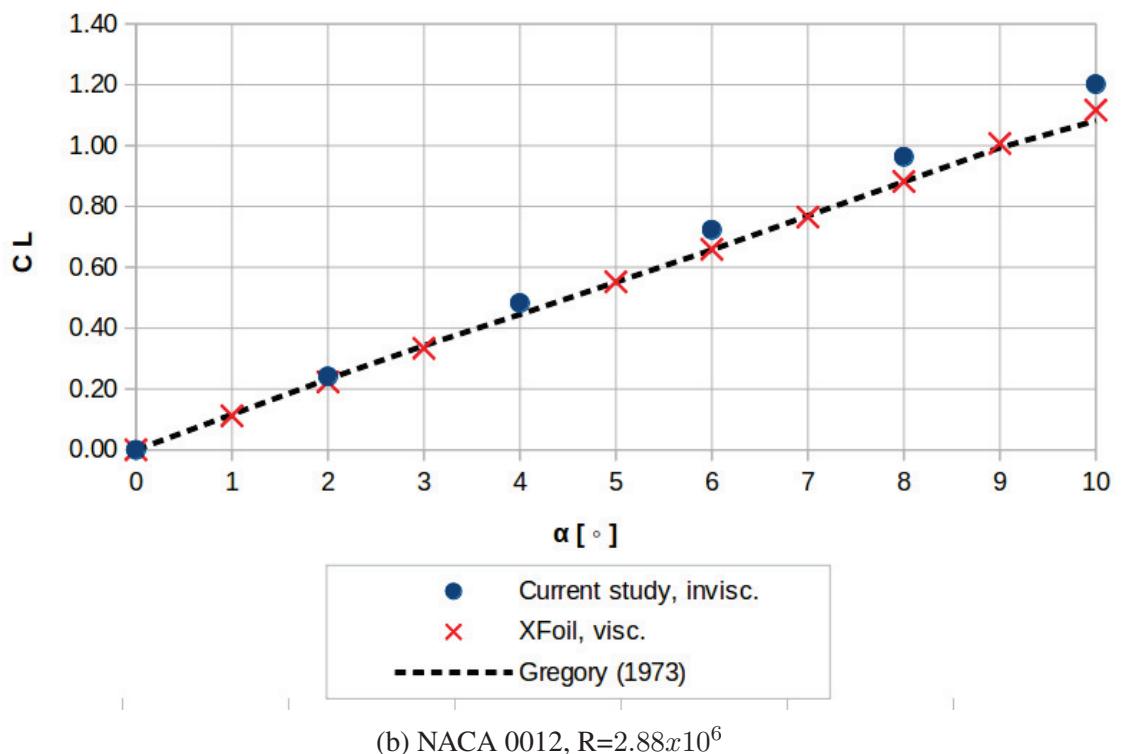
(b) NACA 0012, R=$2.88x10^6$

Figure 3.3. Upper surface transition points at various angle of attacks for NACA 0012 at two different Reynolds numbers, compared with XFoil and Gregory and O'Reilly (1973). *Note that transition points were given by laminar boundary-layer separation after 5 ° angle of attack.*

(a) NACA 0012, R=$1.44x10^6$

(b) NACA 0012, R=$2.88x10^6$

Figure 3.4. Lift coefficients at various angle of attacks for NACA 0012 at two different Reynolds numbers, compared with XFoil and Gregory and O'Reilly (1973)

3.1.2. NACA 0015

NACA 0015 is a symmetrical airfoil and it has 15% maximum thickness to chord ratio and no chamber (Fig. 3.5). The PBS code is compared with Baek and Fuglsang (2009)'s experimental results in the range of 0-10° angle of attacks at $3x10^6$ Reynolds numbers.
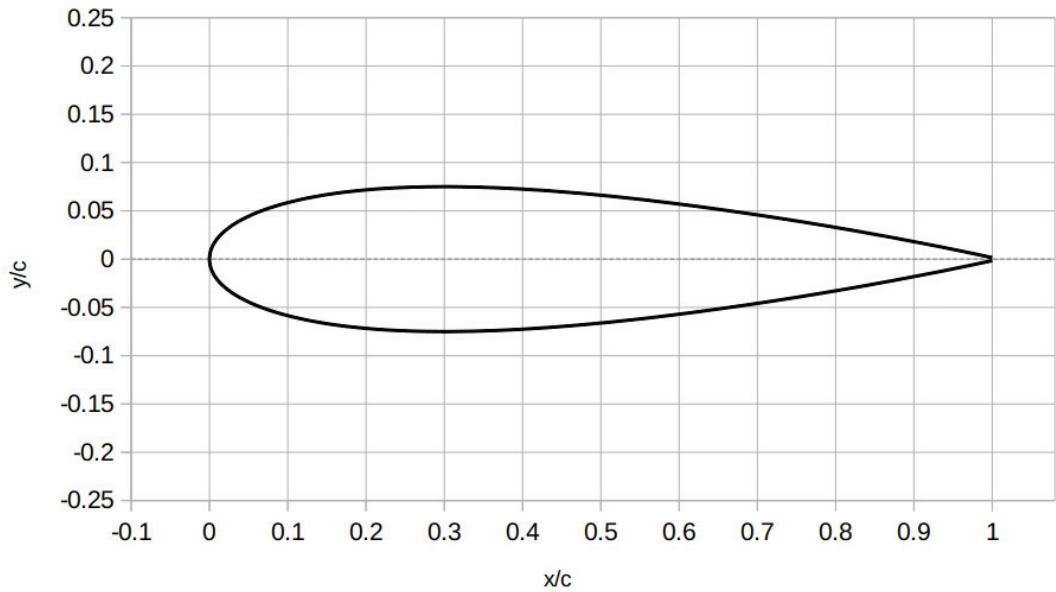

Figure 3.5. NACA 0015 Airfoil

Figure 3.6 compares transition point predictions of current study and XFoil's results with Baek and Fuglsang (2009)'s experimental measurements based on infrared thermography. It is clearly seen that the both numerical results are very close to experimental data. It was taken same critical value, $n_{crit} = 7$, for current study and XFoil. In present study, above 6° angle of attack, the transition point was predicted by laminar separation, not the e^n method since the prediction of the onset of transition with e^n method must be replaced with assumption that the onset of transition corresponds to the separation location at high angle of attacks and high Reynolds numbers for such a moderate thick airfoil (Cebeci and Cousteix (2005)).
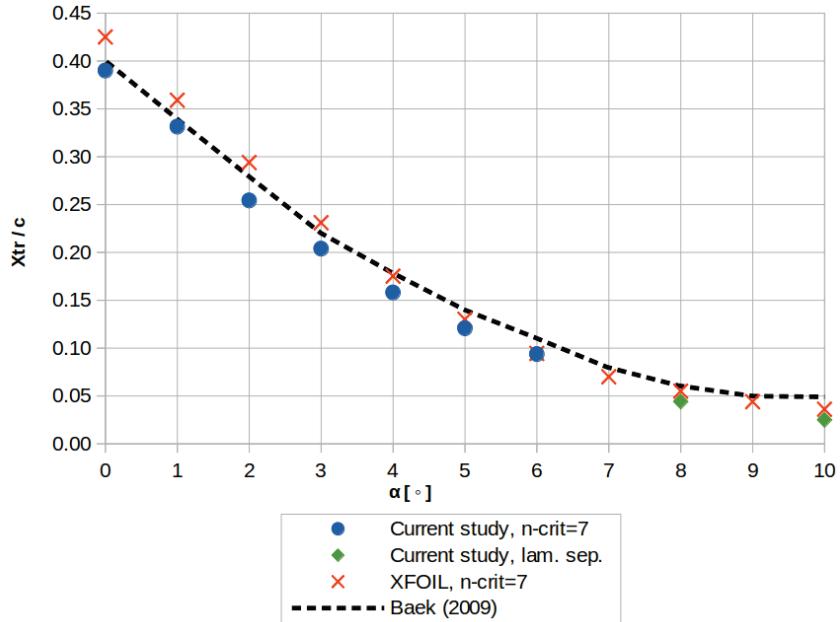
Figure 3.6. Upper surface transition points for NACA 0015 at $R = 3x10^6$, compared with XFoil result and Baek and Fuglsang (2009)'s experimental work. *Note that transition points were given by laminar boundary-layer separation after 7 ° angle of attack.*

3.2. Wind Turbine Airfoils

Today, the seventies wind turbine dedicated airfoils are available in literature and by blade designers. Many airfoils were experimentally verified in wind tunnels up to Reynolds numbers of 3 to 4 million or were numerically verified in RANS simulations or codes at Reynolds numbers higher than 4 million. Above 4 million, testing experimentally is very expensive because of requirement of a large atmospheric, pressure and cryogenic tunnels (Timmer (2009)). Blade designers must rely on airfoil analysis codes such as XFoil or 2D N-S solvers (i.e. EllipSys2D) or RFOIL, which is modified version of XFoil. In RFOIL, XFoil's boundary-layer equations are modified for better stall performance and to count the 3D rotating effects. RFOIL has been used since 1995. Timmer and van Rooji (2003) summarized design of Delft University (DU) wind turbine airfoils and investigated DU airfoils aerodynamics characteristics using XFoil and RFOIL. Application of RFOIL on very high Reynolds numbers wind turbine rotor design can be found in the paper of Ceyhan (2012). Studies about better drag and lift predictions using RFOIL can be found in the papers of Ramanujam et al. (2016) and Ramanujam and Ozdemir (2017).

Wind turbine catalogue is prepared by Bertagnolio et al. (2001) in DTU. This extensive catalogue involves collection of experimental results from different sources and computational results from 2D N-S solvers EllipSys2D code for 6 different airfoil families including NACA 5-digits series, RISO-A1-xx series, FFA-W3-xxx series, NREL's Sxxx series, FX airfoil and DU xx-W-xxx series. As all profiles of airfoil family are given in the catalogue, it compares numerical results with experimental data in terms of lift, drag and skin-friction coefficients, and pressure coefficient distributions for various angle of attacks at different Reynolds numbers.

Figure 3.7 shows contours of wind turbine dedicated airfoils, which have different maximum thickness to chord ratio: 18%, 25% and 40%, NACA 64-618, DU91W250 and DU4050, respectively. The first two airfoils was designed to have high lift-to-drag ratio, which requires laminar flow up to nearly half of the chord length.

The lift coefficients and transition points from PBS code are compared with Baek and Fuglsang (2009)'s experimental results and XFOIL results in the range of 0-10° angle of attacks at $3x10^6$ Reynolds numbers.

NACA 64-618
tip section
t/c=18 %

DU91W250
mid-section
t/c =25 %

DU4050
root section
t/c=40 %
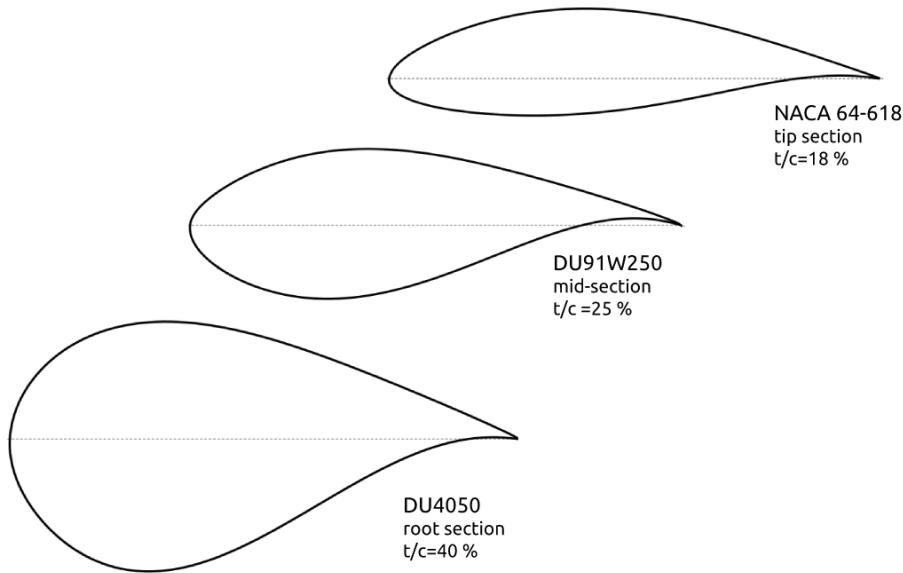
Figure 3.7. Three different airfoils dedicated for wind turbine applications. From root section to tip section of NREL 5 MW Rotor blade.

3.2.1. NACA 64-618

NACA 64-618 has been developed for aviation applications, it is also used at tip of the wind turbine blades. Actually, this 6-digit series airfoil family has been designed for very high lift-to-drag ratio, however, it has high drag value outside operating conditions and shows poor stall behavior. Therefore, it is generally used at the blade tip, which have the high speed portion of the wind turbine blade.
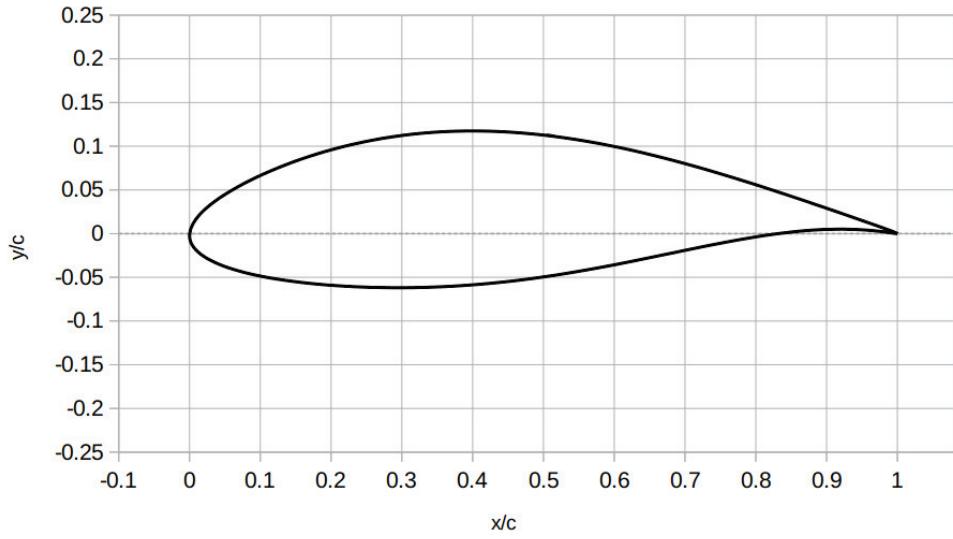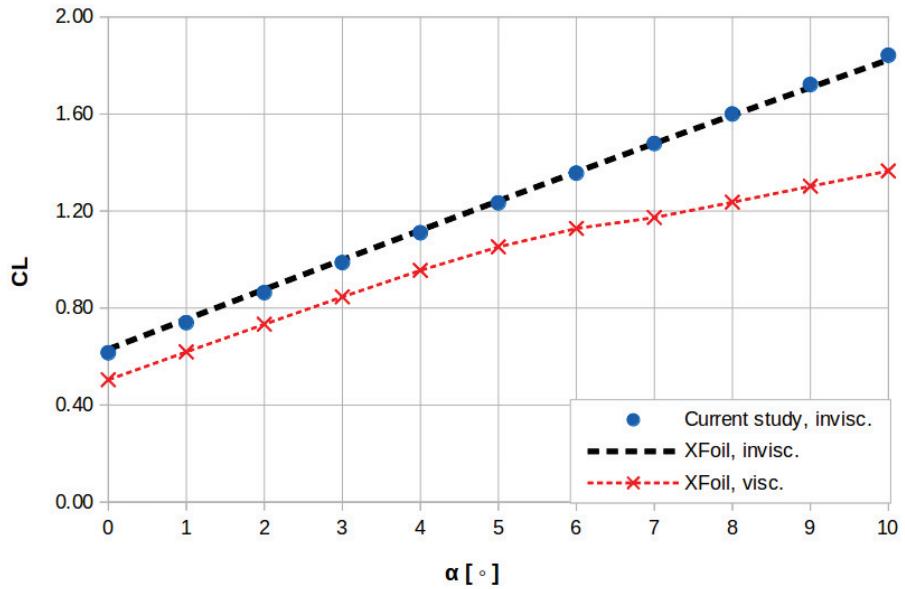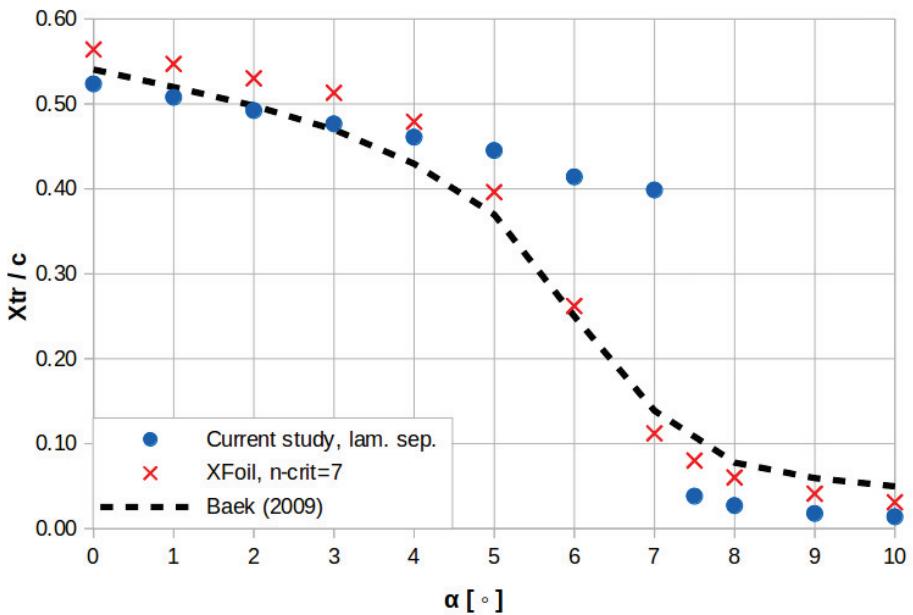

Figure 3.8. NACA 64-618 Airfoil

Lift coefficient and transition points are given as function of angle of attacks at 3 million Reynolds number using PBS code. In Figure 3.9, results are compared with XFoil results and experimental measurements. For XFoil and PBS calculations, n_{crit} is set to 7. In Figure 3.9a, lift coefficient values show exact matching for PBS results (*blue dot*) and XFoil inviscid results (*black dashed line*) despite PBS panel code and XFoil's panel code rely on completely different method. On the other hand, there is a gap between XFoil's viscous lift values (*red cross*) and PBS inviscid lift values and this gap increases at high angle of attacks. In Figure 3.9b, NACA 64-618 has a turning point after 5° angle of attack, which has dramatic decreases in transition locations. PBS code gives good results in terms of transition points except in the range of 5 and 7 degrees. In this range, transition location was highly overestimated. Below 5 degree, the results are very satisfactory despite above 7 degree, they are slightly underestimated.

(a) Lift coefficients, NACA 64-618, R=$3x10^6$

(b) Transition points, NACA 64-618, R=$3x10^6$

Figure 3.9. Lift coefficients and transition points as function of angle of attack for NACA 64-618, compared with XFoil and Baek and Fuglsang (2009)'s infrared thermography measurements. *Note that transition points were given by laminar boundary-layer separation.*

3.2.2. DU91W250

The 25% thick airfoil DU91W250 was specifically designed by W.A. Timmer for wind turbines and the validation of the airfoil was performed in the low-speed low-turbulence wind tunnel in Delft University. The airfoil is widely used on the midsections of the blades. It has large portion of laminar flow where peak lift coefficient of about 1.5, relatively smooth stall and insensitivity to roughness but it was found that it is very sensitive to leading edge roughness by Baek (2008).
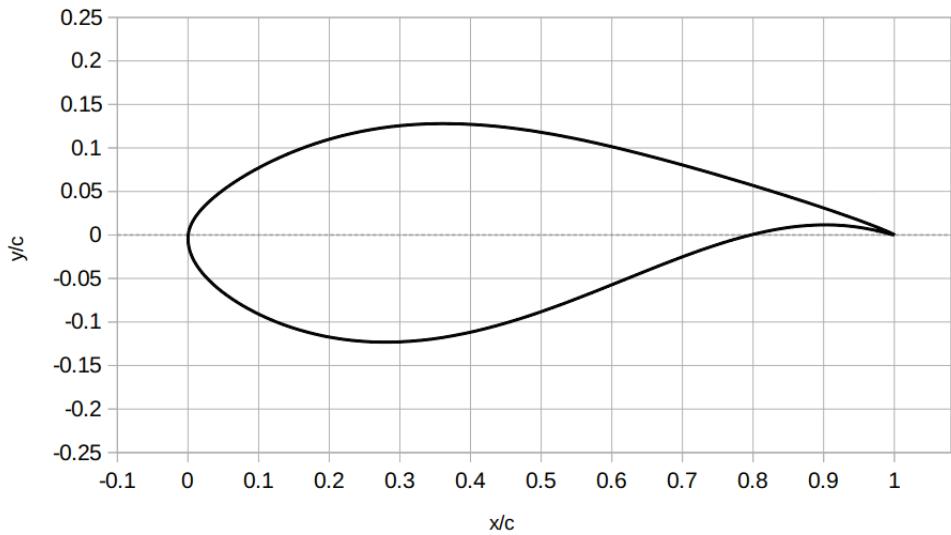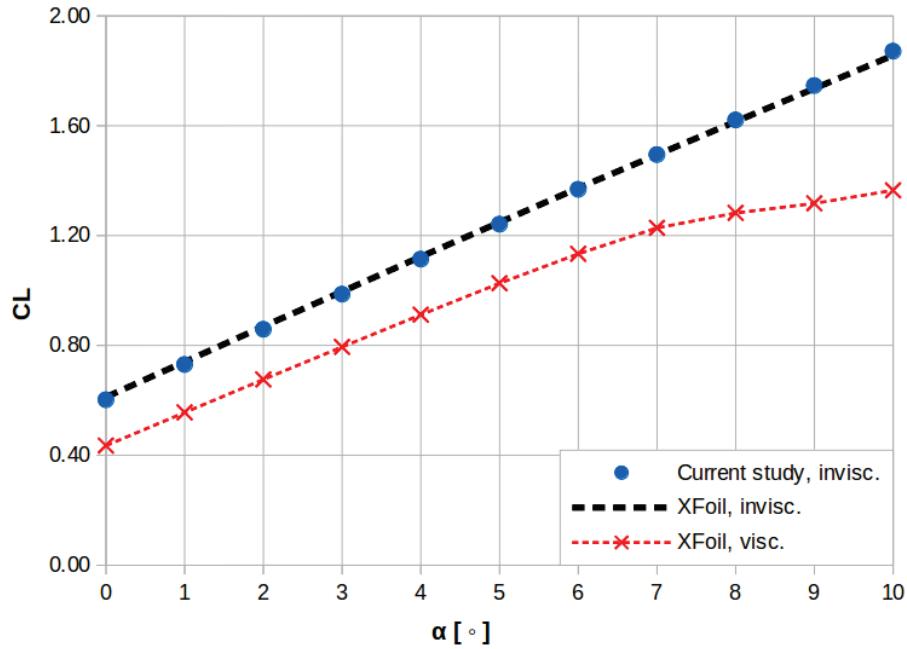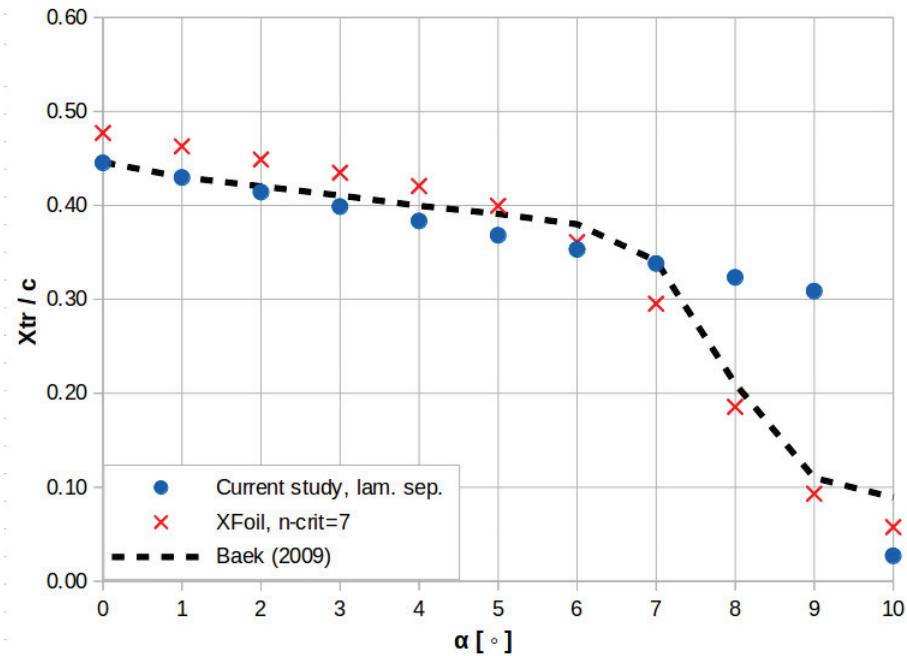

Figure 3.10. DU91W250 Airfoil

Similar to NACA 64-618, it can make same discussion for DU91W250 about Figure 3.11. Although there is a distinct gap between PBS inviscid solution and XFoil viscous solution, both both XFoil's inviscid solution and PBS panel code give same lift coefficients. In Figure 3.11b, DU91W250 has a turning point after 7° angle of attack, which has dramatic decreases in transition location but this turning point is delayed compared to NACA 64-618. Similarly, PBS code gives good results in terms of transition points except for 8 and 9 degrees. In this angle of attacks, transition location was highly over-predicted. However, below 8 degrees, the results are very close to experimental measurements.

(a) Lift coefficients, DU91W250, R=$3x10^6$

(b) Transition points, DU91W250, R=$3x10^6$

Figure 3.11. Lift coefficients and transition points as function of angle of attack for DU91W250, compared with XFoil and Baek and Fuglsang (2009)'s infrared thermography measurements. *Note that transition points were given by laminar boundary-layer separation.*

3.2.3. DU4050

The very thick DU4050 airfoil has nearly cylinder shape and it is used on blade root. The thickest airfoil of DUxx family has also different thickness variations and designed in Delft University.
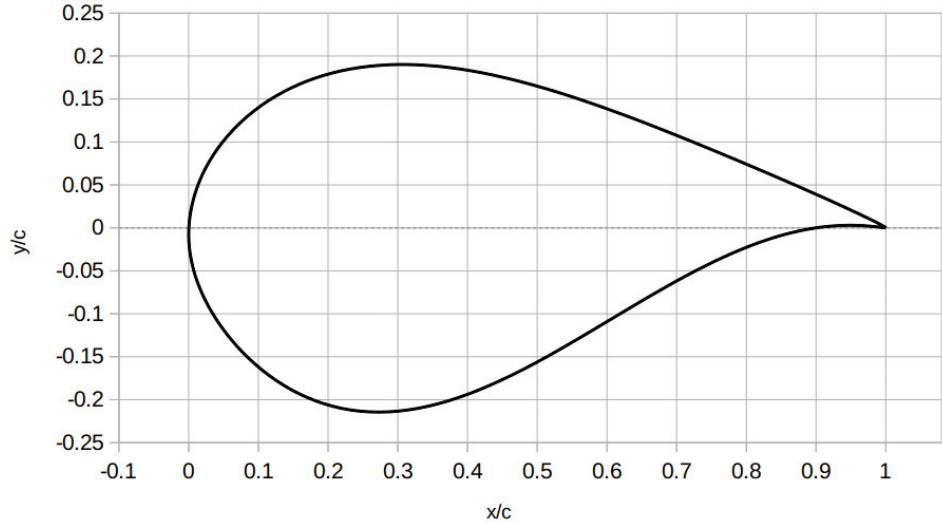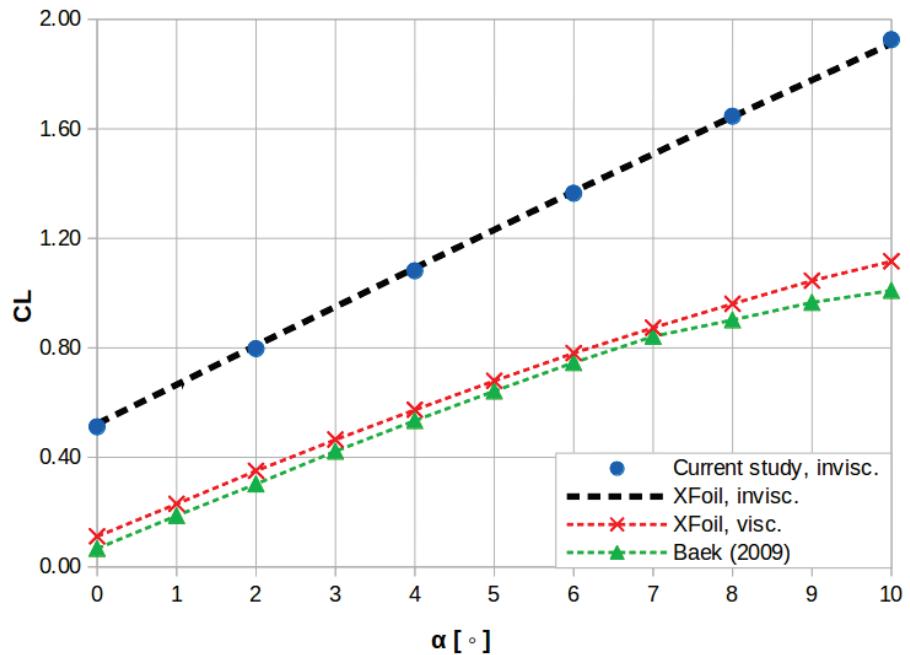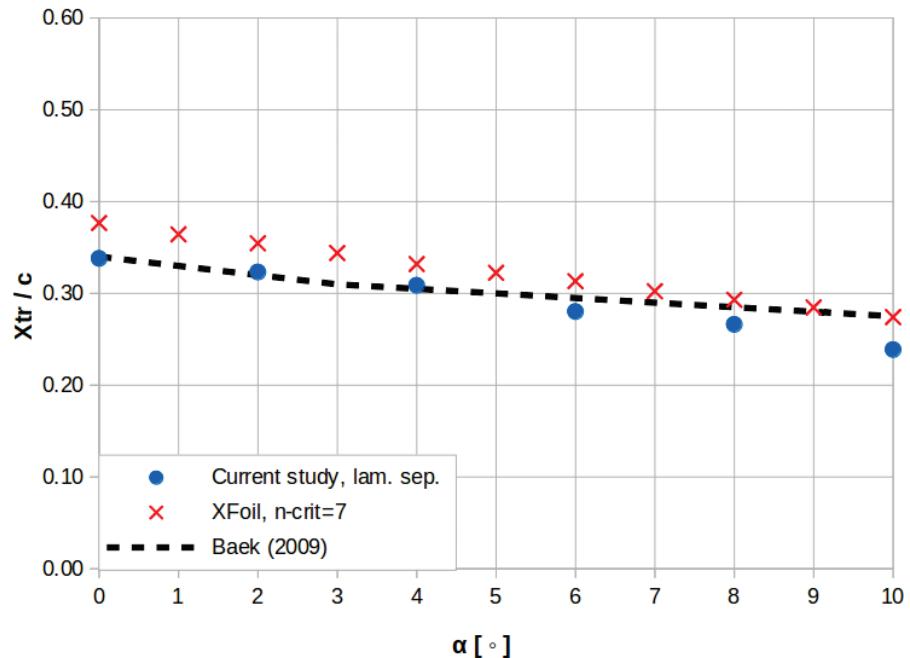

Figure 3.12. DU4050 Airfoil

Figure 3.13a compares lift coefficient values. Although the same discussion on previous two airfoils is still valid on this airfoil, experimental lift coefficient values clearly show that inviscid lift values from panel code are completely unrealistic for such a thick airfoil. Also, XFoil slightly overestimates lift coefficients at especially above 8 degrees angle of attack despite it uses interactive boundary-layer method. In Figure 3.13b, DU4050 has no turning point in transition location unlike NACA 64-618 and DU91W250. Transition location linearly moves towards leading edge. Again, PBS code gives good results in terms of transition points but in the all range of angle of attacks.

(a) Lift coefficients, DU4050, R=$3x10^6$

(b) Transition points, DU4050, R=$3x10^6$

Figure 3.13. Lift coefficients and transition points as function of angle of attack for DU4050, compared with XFoil and Baek and Fuglsang (2009)'s infrared thermography measurements. *Note that transition points were given by laminar boundary-layer separation.*

CHAPTER 4

EPILOGUE

4.1. Concluding Remarks

Airfoil laminar boundary-layer stability calculations were performed and transition point is predicted based on a semi-empirical method. The used method to predict transition is called as e^n method and it is based on linear stability theory. This method requires solution of stability equations and laminar boundary-layer equations. Both 2D stability and 2D laminar boundary-layer equations in differential form with appropriate boundary conditions were numerically solved. The required pressure distribution was obtained from inviscid panel code based on Hess-Smith method.

Three FORTRAN codes, HSPM (panel code), BLP2D (2D boundary-layer code) and STP2D (2D stability code) were connected to each other via inputs-outputs in the one code, called as PBS code. PBS is the abbreviation of **P**anel-**B**oundary layer-**S**tability words.

The PBS code was first validated on NACA 0012 and NACA 0015 airfoils making comparison with numerical and experimental works in literature. It was seen that the code was qualified for transition point prediction with many stability and boundary-layer outputs. It was seen that amplified disturbance frequency magnitude, amplification starting point and choice of threshold value are key points to correctly predict transition point for e^n method.

After validation, three different thick airfoils dedicated for wind turbine applications were analyzed in terms of lift coefficient and transition location, namely NACA 64-618, DU91W250 and DU4050. The results were compared with XFoil's viscous and inviscid solutions and experimental wind tunnel measurements.

Following results were found: First, as airfoil thickness increases, the need for interactive boundary-layer method increases for accurate lift coefficient. However, transition point can be still correctly predicted using inviscid pressure distribution. Second, at high angle of attacks and high Reynolds numbers, laminar boundary-layer separation

point can be directly taken as transition point instead of using the e^n method.

Disadvantages of PBS code can be listed as follows: First, to give pressure (or edge-velocity) distribution without interactive method. This leads to incorrect lift prediction. Second, to make initial guess for α and ω. The initial guesses must be found logically to obtain converged results. Guess initial values are taken by trail and error from Blasius flow (zero pressure gradient) stability diagram depends on stability Reynolds number. While trial and error method usually works, improper selection of α and ω results diverged solution.

4.2. Suggestions for Future Work

Despite author of the Master's thesis has tried to give as far as a satisfactory work in terms of an academic study about the subject of airfoil inviscid-viscous solution and transition prediction based on linear stability theory, one can develop a more complete study using this future recommendations:

- Transform FORTRAN codes to MATLAB script with all inputs-outputs to make quicker analysis and better post-processing.

- Use one of the interactive boundary-layer methods in available literature to obtain improved pressure distribution. This requires a loop between panel code and boundary-layer code (Figure 4.1).
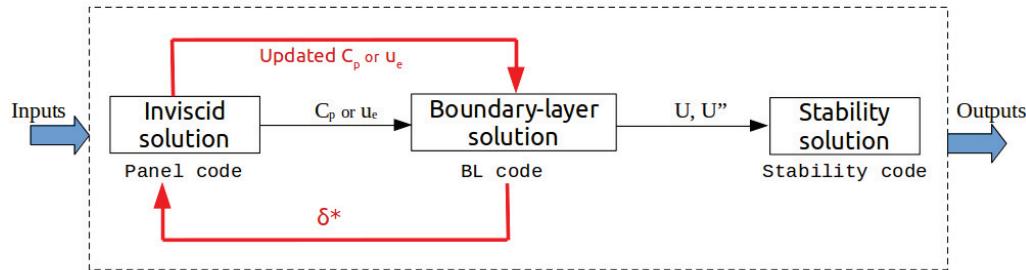

Figure 4.1. Modified short flow diagram for interactive method

- Include RFOIL analysis as well as XFOIL results to compare RFOIL's improvements.

- Modify boundary conditions in stability code to study laminar flow control using mass transfer such as blowing and suction.

- Make wake calculation to be able to predict drag coefficient. Although one of the boundary-layer code outputs is local skin-friction coefficient along airfoil chord, this is just one part of the total drag. Total drag, C_D, is summation of skin-friction (C_{df}) and pressure drag (C_{dp}).

$$C_D = C_{df} + C_{dp} \tag{4.1}$$

As explain in the XFoil manuel, drag coefficient is obtained by applying the Squire-Young equation at last point in the **wake**, not at the trailing edge (See Eq. 4.2). All variables in the Eq. 4.2, namely momentum thickness, shape factor and edge-velocity, come from end of the wake. Typically, the last point of the wake is taken as 1 chord downstream as shown in Fig. 4.2.

$$C_D = 2\theta(u_0/U)^{\frac{H+5}{2}} \tag{4.2}$$
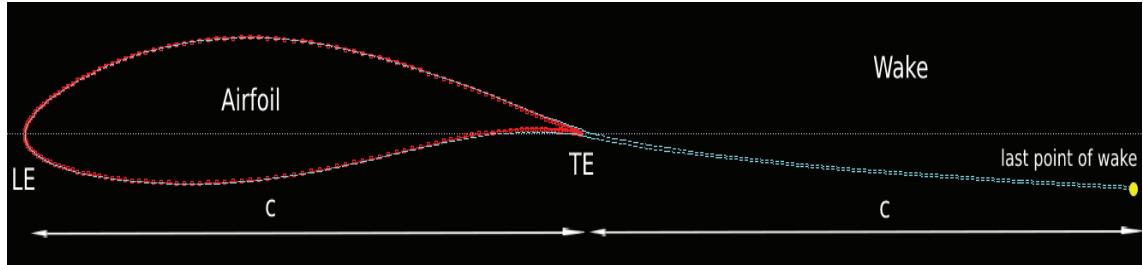
Figure 4.2. Wake behind airfoil. Blue dashed line indicates boundary-layer. *Adapted from XFOIL program.*

REFERENCES

Baek, P. (2008). *Experimental Detection of Laminar to Turbulent Boundary-layer Transition In An Industrial Wind Tunnel Facility*. MSc. Thesis, Department of Mechanical Engineering, Technical University of Denmark.

Baek, P. and P. Fuglsang (2009). *Experimental Detection of Transition On Wind Turbine Blades*. In EWEC 2009, Marseille.

Bertagnolio, F., N. Sorensen, J. Johansen, and P. Fuglsang (2001). *Wind Turbine Airfoil Catalogue*. Denmark. Forskningscenter Risoe. Risoe-R, No. 1280(EN).

Cebeci, T. and J. Cousteix (2005). *Modeling and computation of boundary-layer flows: laminar, turbulent and transitional boundary layers in incompressible and compressible flows*. Horizons Pub.

Ceyhan, O. (2012). *Towards 20MW Wind Turbine: High Reynolds Number Effects on Rotor Design*. 47th AIAA Aerospace Sciences, Tennessee.

Drela, M. (1989). *XFOIL: An Analysis and Design System for Low Reynolds Number Airfoils*. Low Reynnolds Number Aerodynamics. Springer-Verlag Lec. Notes in Eng. 54.

Drela, M. and M. B. Giles (1987). *Viscous-Inviscid Analysis of Transonic and Low Reynolds Number Airfoils*. AIAA Journal, Vol. 25, No.10.

Fielding, S. (2008). *Hydrodynamic Stability. Part I: Linear stability analysis. Section 4: Shear flow instability*. Lecture Notes, Durham University.

Gregory, N. and C. O'Reilly (1973). *Low-Speed Aerodynamics Characteristics of NACA 0012 Aerofoil Section*. Aerodynamics Division N.P.L., Reports and Memoranda No. 3726.

Mack, L. M. (1977). *Transition and Laminar Instability*. In AGARD Laminar-Turbulent

Transition, Vol. 1.

Mack, L. M. (1984). *Boundary-Layer Linear Stability Theory*. AGARD Report No: 709, Part 3, California Institute of Technology.

Mersinligil, M. (2006). *Airfoil Boundary Layer Calculations Using Interactive Method and e^n Transition Prediction Technique*. Master's Thesis, METU, Ankara.

Moran, J. (1984). *An Introduction To Therotical and Computational Aerodynamics*. John Wiley & Sons.

Ozgen, S. (1994). *Interactive Boundary Layer Calculations Over An Airfoil and Its Resulting Wake*. Master's Thesis, METU, Ankara.

Panton, R. L. (1996). *Incompressible Flow*. John Wiley & Sons.

Ramanujam, G. and H. Ozdemir (2017). *Improving Airfoil Lift Prediction*. 35th Wind Energy Symposium, AIAA SciTech, Texas.

Ramanujam, G., H. Ozdemir, and H. Hoeijmakers (2016). *Improving Airfoil Drag Prediction*. 34th Wind Energy Symposium, AIAA SciTech, California.

Rosenhead, L. (1963). *Laminar Boundary Layers*. Oxford University Press.

Russo, S., D. D. Rosa, R. S. Donelli, and C. de Nicola (2018). *The Use of RANS Approach for Predicting Transition*. Aerotecnica Vol.97, No.3, July-September 2018.

Schlichting, H. and K. Gersten (2017). *Boundary-Layer Theory*. Springer.

Sheng, C. (2017). *Advances in Transitional Flow Modeling*. Springer.

Silisteanu, P.-D. and R. M. Botez (2010). *Transition-Flow-Occurrence Estimation: A New Method*. Journal of Aircraft, AIAA.

Smith, L. (2011). *An Interactive Boundary Layer Modelling Methodology for Aerodynamic Flows*. Master's Thesis, University of Pretoria.

Timmer, W. (2009). *An Overview of NACA 6-digit Airfoil Aeries Characteristics with Reference to Airfoils for Large Wind Turbine Blades*. 47th AIAA Aerospace Sciences, Florida.

Timmer, W. and R. van Rooji (2003). *Summary of the Delft University Wind Turbine Dedicated Airfoils*. Journal of Solar Energy Engineering, ASME, Vol. 125.

van Ingen, J. (2008). *The e^n Method for Transition Prediction. Historical Review of Work at TU Delft*. 38th Fluid Dynamics Conference and Exhibit, Washington, AIAA.

Wanthanadamkerng, T. (2017). *CFD modelling of an airfoil section equipped with Vortex generators*. Master's Thesis, Technical University of Denmark.

White, F. M. (1991). *Viscous Fluid Flow*. McGraw-Hill.

APPENDIX A

PBS CODE FLOW DIAGRAM

PBS code is the combination of following three codes: panel code (**HSPM.f**), boundary-layer code (**blp2d.for**) and stability code (**stp2d.f**). Flow diagram of the combined code (PBS code) is given in Fig. A.1 and the code inputs-outputs are explained in detail.
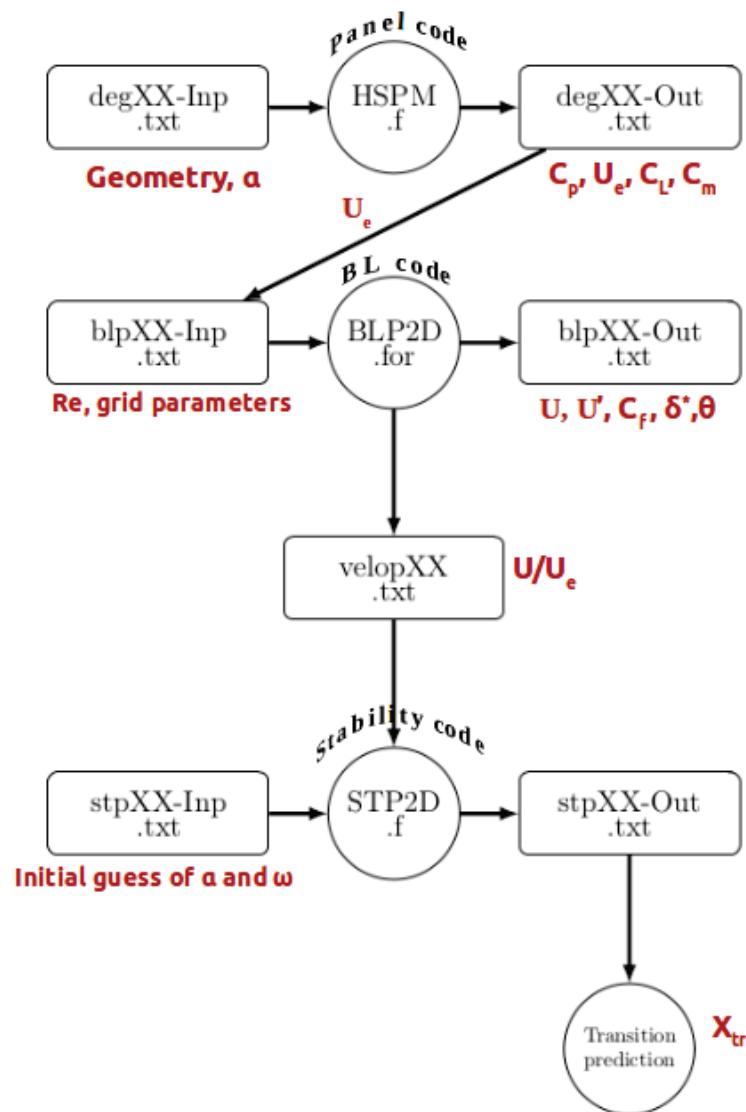

Figure A.1. PBS code flow diagram with explained inputs-outputs boxes.

——-

HSPM.f: Hess-Smith panel code written in Fortran 77. It contains one MAIN and four subroutines.

——-

degXX-Inp.txt: Panel code input file. It requires following inputs:

NODTOT - - - total number of panels

X(1) ... X(NODTOT+1) - - - x-coordinates

Y(1) ... Y(NODTOT+1) - - - y-coordinates

ALPHA - - - the angle of attack.

degXX-Out.txt: Panel code output file. It gives following outputs:

X(J) - - - panel x-coordinates

Y(J) - - - panel y-coordinates

CP(J) - - - pressure coefficient

UE(J) - - - edge-velocity

CL - - - lift coefficient

CM - - - pitch-moment coefficient

——-

BLP2D.for: Boundary-layer code written in Fortran 95. It contains one MAIN and seven subroutines.

——-

blpXX-Inp.txt: Boundary-layer code input file. It requires following inputs:

NXT - - - The number of x-stations

NPT - - - The number of normal grid points

X(I) - - - The x-coordinate of geometry

Y(I) - - - The y-coordinate of geometry

UE(I) - - - The edge-velocity

RL - - - Reynolds number

XCTR - - - Transition location

ETAE - - - The transformed boundary layer thickness

VGP - - - The variable grid parameter

DETA(1) - - - The size of first normal grid

P2(1) - - - Initial pressure at first x-station

blpXX-Out.txt: Boundary-layer code output file. It gives following outputs:

At each x-station:

ETA - - - Normal grid points

F - - - Dimensionless stream function

U - - - Dimensionless velocity profile

V - - - Derivative of dimensionless velocity

B - - - Turbulent BL parameter

XSEP - - - Seperation point

Summary results:

UE - - - Dimensionless velocity

DELS - - - Dimensionless displacement thickness

THETA - - - Dimensionless momentum thickness

VW - - - Dimensionless wall shear

CF - - - Local skin-friction coefficient

RTHETA - - - Reynolds number based on momentum thickness

velopXX.txt: Boundary-layer code second output file. It is used for stability code as an input. It contains dimensionless velocity profiles at each x-station along the geometry.

_____-

STP2D.f: Stability code written in Fortran 77. It contains one MAIN and four subroutines.

_____-

stpXX-Inp.txt: Stability code input file. It requires following inputs:

NXT - - - The number of x-station

NX0 - - - Transition search starting station

IXT - - - Number of lines. (0, compute neutral stability curve only.)

UINF - - - The free-stream velocity

BIGL - - - The reference length

RL - - - The Reynolds number based on reference length

ALFA - - - initial eigenvalue guess of wave-number

OMEGA - - -initial eigenvalue guess of wave-frequency

X(I) - - - The x-coordinate

S(I) - - - The surface distance

UE(I) - - - The edge-velocity

stpXX-Out.txt: Stability code output file. It gives following outputs:

RX - - - The Reynolds number based on x-station

REY - - - The stability Reynolds number

At each stability line for a fixed physical frequency (ω):

PHYSICAL ALFA - - - Converged real and imaginary parts of wave-number

CLOGA - - - The integrated amplification factor

The Fortran codes are compiled in Simply Fortran 3.2 under Ubuntu 18.04 LTS (See Fig. A.2). However, it is not requisite, one can run the codes using any suitable Fortran compiler under any operating system.

Figure A.2. Stability code in Simply Fortran compiler

APPENDIX B
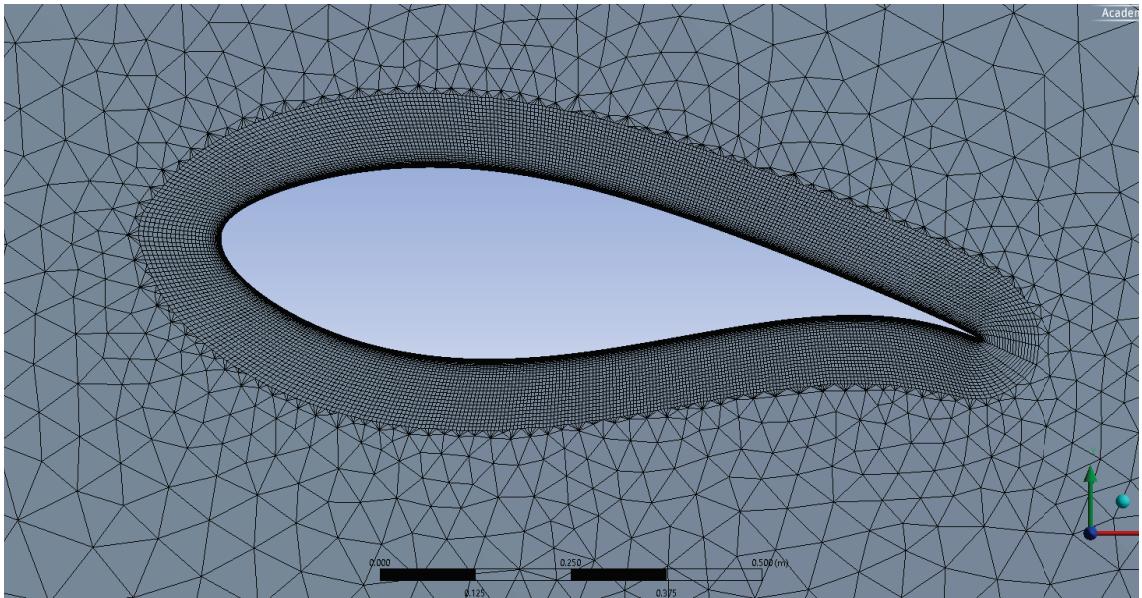
CFD SIMULATION OF DU91W250 AIRFOIL

CFD simulation is performed for DU91W250. Free-stream velocity is 47 m/s and angle of attack is 8°. Based on 1 m chord length, Reynolds number is $R = 3x10^6$. The C-type mesh is used. The distances from the computational domain boundaries to the airfoil are 14 chord lengths from outlet and 7 chord lengths from inlet. The generated mesh consists of 143,349 structured grid cells. First layer height at the boundary-layer mesh is 8.2e-06 m providing wall y+ values of approximately 1.0. The Transition SST turbulence model is employed. This four-equation turbulence model is based on the SST k-ω model and two transport equations for the intermittency and for the transition onset criteria.

The mesh views are presented in Figure B.1. Velocity & pressure contours are given in Figure B.2. Explanations on figures can be found in the sub-figure caption.
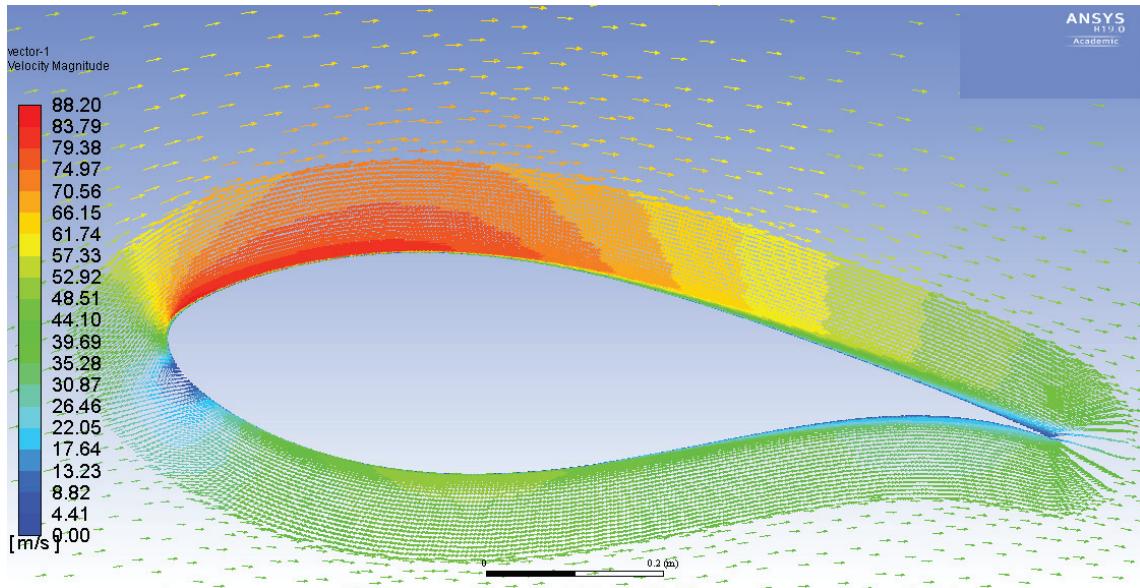
(a) General mesh view. Computational fluid domain is taken as 7 chord from inlet and 14 chord from outlet.
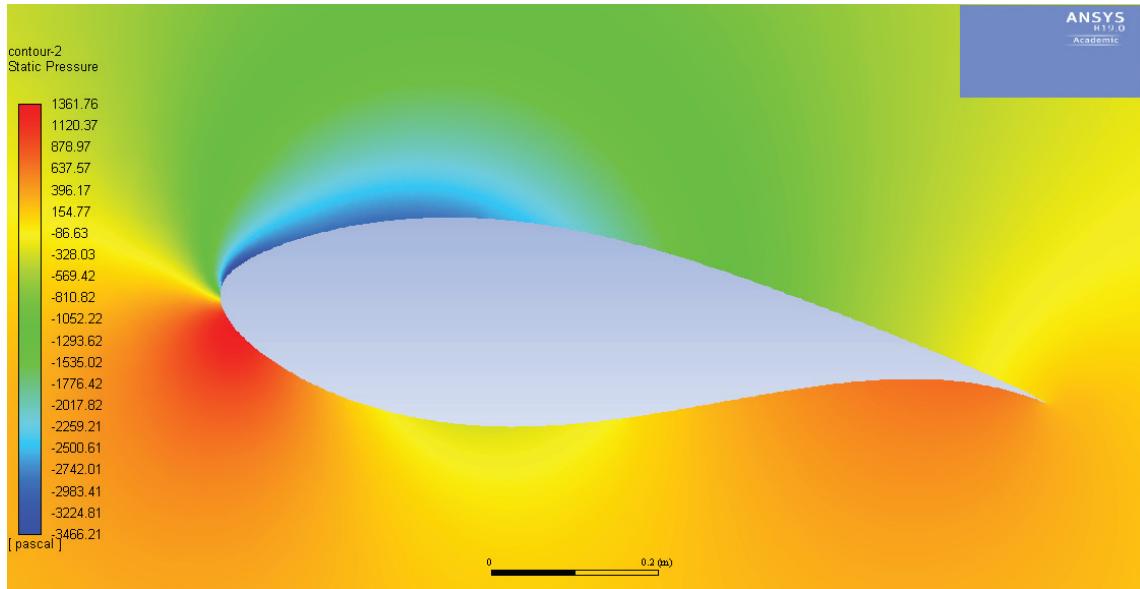

(b) Boundary-layer mesh view. Close region of airfoil surface.

Figure B.1. Mesh views for DU91W250, $R = 3x10^6$, $\alpha = 8°$.

(a) Velocity contours. Blue region below the leading edge indicates stagnation point. Note that on the upper surface, velocities in streamwise direction are gradually decreased as boundary-layer thickness increases, red color turns orange, yellow and green.

(b) Static pressure contours. Note that upper surface pressure values are negative, it indicates lower pressure than free-stream. Also, upper surface pressure is recovered after some point, blue region turns green and yellow.

Figure B.2. Pressure contours and velocity vectors for DU91W250, $R = 3x10^6$, $\alpha = 8°$.